



**HAL**  
open science

## Visible/near-infrared spectral diversity from in situ observations of the Bagnold Dune Field sands in Gale Crater, Mars

Jeffrey Johnson, Cherie Achilles, James Bell, Steve Bender, Edward Cloutis, Bethany L Ehlmann, Abigail Fraeman, Olivier Gasnault, Victoria Hamilton, Stéphane Le Mouélic, et al.

### ► To cite this version:

Jeffrey Johnson, Cherie Achilles, James Bell, Steve Bender, Edward Cloutis, et al.. Visible/near-infrared spectral diversity from in situ observations of the Bagnold Dune Field sands in Gale Crater, Mars. *Journal of Geophysical Research. Planets*, 2017, 122 (12), pp.2655-2684. 10.1002/2016JE005187 . hal-02343905

**HAL Id: hal-02343905**

**<https://hal.science/hal-02343905>**

Submitted on 3 Jan 2022

**HAL** is a multi-disciplinary open access archive for the deposit and dissemination of scientific research documents, whether they are published or not. The documents may come from teaching and research institutions in France or abroad, or from public or private research centers.

L'archive ouverte pluridisciplinaire **HAL**, est destinée au dépôt et à la diffusion de documents scientifiques de niveau recherche, publiés ou non, émanant des établissements d'enseignement et de recherche français ou étrangers, des laboratoires publics ou privés.

Copyright

## RESEARCH ARTICLE

10.1002/2016JE005187

## Special Section:

Investigations of the Bagnold Dune Field, Gale crater

## Key Points:

- Visible/near-infrared spectra of Bagnold Dunes sands indicate variable mixtures of olivine and ferric materials
- Observed spectral variations with grain size are consistent with laboratory spectra of olivine
- Coarse-grained fractions enriched in mafic components compared to more ferric, fine fractions, likely related to aeolian/kinematic sorting

## Correspondence to:

J. R. Johnson,  
Jeffrey.R.Johnson@jhuapl.edu

## Citation:

Johnson, J. R., et al. (2017), Visible/near-infrared spectral diversity from in situ observations of the Bagnold Dune Field sands in Gale Crater, Mars, *J. Geophys. Res. Planets*, 122, 2655–2684, doi:10.1002/2016JE005187.

Received 3 OCT 2016

Accepted 10 JAN 2017

Published online 13 DEC 2017

## Visible/near-infrared spectral diversity from in situ observations of the Bagnold Dune Field sands in Gale Crater, Mars

Jeffrey R. Johnson<sup>1</sup> , Cherie Achilles<sup>2</sup> , James F. Bell III<sup>3</sup> , Steve Bender<sup>4</sup>, Edward Cloutis<sup>5</sup> , Bethany Ehlmann<sup>6,7</sup> , Abigail Fraeman<sup>6</sup> , Olivier Gasnault<sup>8,7</sup> , Victoria E. Hamilton<sup>9</sup> , Stéphane Le Mouélic<sup>10</sup>, Sylvestre Maurice<sup>8</sup>, Patrick Pinet<sup>8</sup> , Lucy Thompson<sup>11</sup> , Danika Wellington<sup>3</sup>, and Roger C. Wiens<sup>12</sup>

<sup>1</sup>The Johns Hopkins University Applied Physics Laboratory, Laurel, Maryland, USA, <sup>2</sup>Department of Geoscience, University of Arizona, Tucson, Arizona, USA, <sup>3</sup>School of Earth and Space Exploration, Arizona State University, Tempe, Arizona, USA, <sup>4</sup>Planetary Science Institute, Tucson, Arizona, USA, <sup>5</sup>Department of Geography, University of Winnipeg, Winnipeg, Manitoba, Canada, <sup>6</sup>Jet Propulsion Laboratory, California Institute of Technology, Pasadena, California, USA, <sup>7</sup>Division of Geological and Planetary Sciences, California Institute of Technology, Pasadena, California, USA, <sup>8</sup>Institut de Recherche en Astrophysique et Planétologie, Université de Toulouse, CNRS, Toulouse, France, <sup>9</sup>Southwest Research Institute, Boulder, Colorado, USA, <sup>10</sup>Laboratoire de Planétologie et Géodynamique, Université de Nantes, Nantes, France, <sup>11</sup>Planetary and Space Science Centre, University of New Brunswick, Fredericton, New Brunswick, Canada, <sup>12</sup>Los Alamos National Laboratory, Los Alamos, New Mexico, USA

**Abstract** As part of the Bagnold Dune campaign conducted by Mars Science Laboratory rover Curiosity, visible/near-infrared reflectance spectra of dune sands were acquired using Mast Camera (Mastcam) multispectral imaging (445–1013 nm) and Chemistry and Camera (ChemCam) passive point spectroscopy (400–840 nm). By comparing spectra from pristine and rover-disturbed ripple crests and troughs within the dune field, and through analysis of sieved grain size fractions, constraints on mineral segregation from grain sorting could be determined. In general, the dune areas exhibited low relative reflectance, a weak ~530 nm absorption band, an absorption band near 620 nm, and a spectral downturn after ~685 nm consistent with olivine-bearing sands. The finest grain size fractions occurred within ripple troughs and in the subsurface and typically exhibited the strongest ~530 nm bands, highest relative reflectances, and weakest red/near-infrared ratios, consistent with a combination of crystalline and amorphous ferric materials. Coarser-grained samples were the darkest and bluest and exhibited weaker ~530 nm bands, lower relative reflectances, and stronger downturns in the near-infrared, consistent with greater proportions of mafic minerals such as olivine and pyroxene. These grains were typically segregated along ripple crests and among the upper surfaces of grain flows in disturbed sands. Sieved dune sands exhibited progressive decreases in reflectance with increasing grain size, as observed in laboratory spectra of olivine size separates. The continuum of spectral features observed between the coarse- and fine-grained dune sands suggests that mafic grains, ferric materials, and air fall dust mix in variable proportions depending on aeolian activity and grain sorting.

## 1. Introduction

A comprehensive campaign to provide the first in situ analyses of sand dunes on another planet was conducted by Mars Science Laboratory rover Curiosity between mission days (Martian solar days, sols) 1181 and 1254 (December 2015 to February 2016). The main goals were to provide insights regarding sand provenance and evolution, the geochemical and mineralogical segregation of sands, dune textural characteristics, and their reflection in the rock record [Bridges and Ehlmann, 2017; Ehlmann et al., 2017; Lapotre et al., 2016; Ewing et al., 2017]. By determining the mineralogy and chemistry of the sands associated with the Bagnold Dunes, constraints on the composition of their protoliths could be established. Understanding possible mineral segregation and grain sorting among areas with variable aeolian activity could also improve models of sand and dust mobility, particularly in the context of sand migration observed from orbit for portions of the Bagnold Dunes and in other dune fields [Ayoub et al., 2014; Bridges et al., 2012a, 2012b; Silvestro et al., 2013, 2016; Day and Kocurek, 2016].

For these reasons a key component to the Bagnold Dune campaign was the use of visible/near-infrared (VNIR) spectroscopy to constrain the mineralogy and composition of the dune sands using a combination

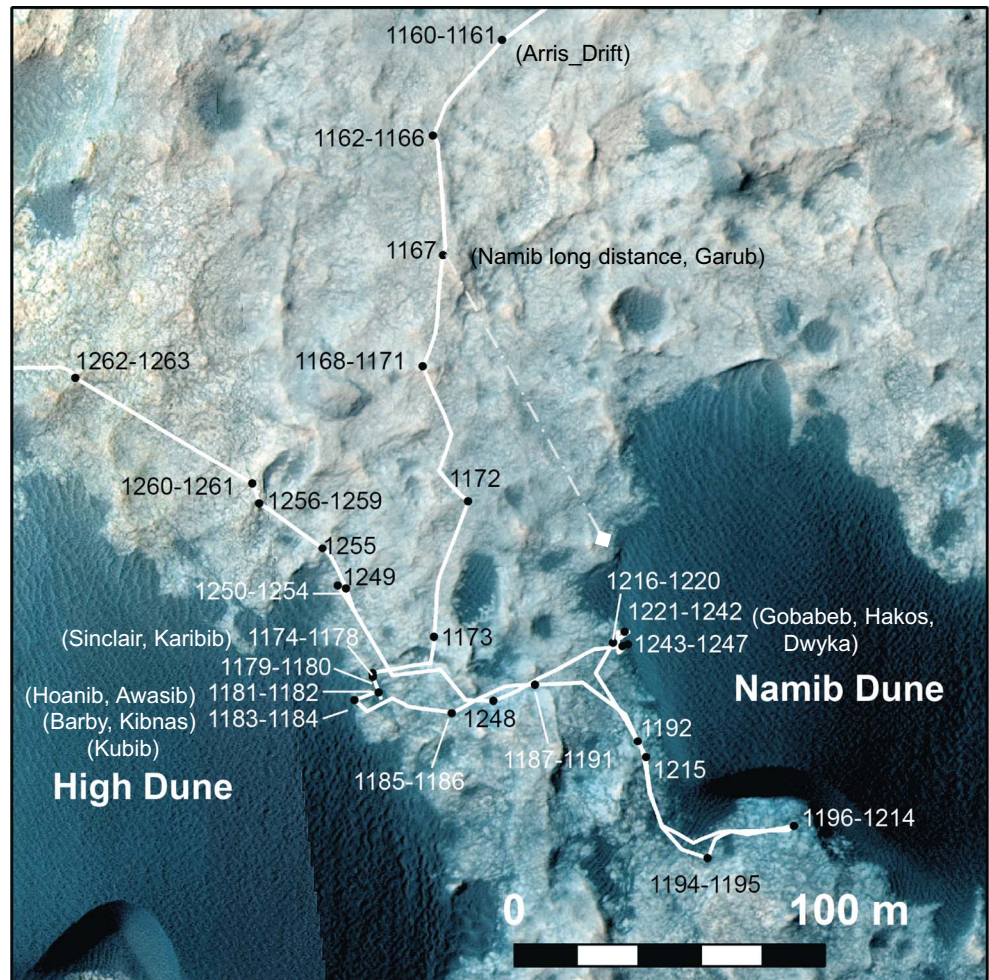


**Figure 1.** Context map (background is HiRISE false-color mosaic) showing Sol number locations of rover stops and targets of interest. Dash-dotted line extending from Sol 1167 location represents view toward Namib Dune acquired from that location. North is toward the top. The Naukluft Plateau is west of this scene.

of Mast Camera (Mastcam) multispectral imaging (445–1013 nm) and Chemistry and Camera (ChemCam) passive point spectroscopy (400–840 nm). This was accomplished by observing pristine and rover-disturbed ripple crests and troughs within the dune field and by analyzing sieved grain size fractions. These in situ analyses provided a companion perspective to orbital spectral observations [e.g., Seelos *et al.*, 2014; Lapotre *et al.*, 2017].

The Bagnold Dune campaign began as the rover approached and observed the northern extent of the dunes (Figure 1). The initial stop was along the eastern edge of High Dune to conduct engineering tests related to rover mobility. The rover then drove to the western edge of Namib Dune and the Gobabeb sampling area for detailed observations, including analysis of sieved sand fractions derived from two separate scoop locations. The first scoop was sieved to  $<150\ \mu\text{m}$  and  $>150\ \mu\text{m}$  size fractions, whereas the second scoop was sieved to  $150\ \mu\text{m}$  to  $1\ \text{mm}$  and  $>1\ \text{mm}$  fractions. A third scoop was intended to provide a second  $150\ \mu\text{m}$  to  $1\ \text{mm}$  portion for delivery to the Sample Analysis at Mars (SAM) instrument, although this activity did not occur owing to an actuator anomaly [Ehlmann *et al.*, 2017]. Afterward the rover drove to rock units of interest near the eastern edge of High Dune, dumped presieved ( $>150\ \mu\text{m}$ ) and postsieved ( $<150\ \mu\text{m}$ ) samples from the third scoop, and continued westward along the northern edge of High Dune toward the Naukluft Plateau. Mastcam multispectral and ChemCam passive measurements were acquired at each of these locations and form the basis of the results presented here.

**Table 1.** ChemCam and Mastcam Sequences Used

Target	Sol	Sequence ID	LTST (Start)	Raster Size (Column × Row)
Arris Drift	1162	ccam01162	12:19	5 × 1
Bagnold (Namib Dune)	1167	ccam01167	12:18	5 × 1
Sinclair	1174	ccam01174	12:22	5 × 1
Karibib	1177	ccam01177	12:23	1 × 10
Awasib	1182	ccam02182	13:08	1 × 5
Hoanib	1182	ccam01182	12:37	1 × 10
Barby	1184	ccam01184	12:35	1 × 5 diagonal
Kibnas	1184	ccam02184	12:51	1 × 5 diagonal
Dump A	1229	ccam02228	12:52	5 × 1
Dump B	1229	ccam01228	12:46	5 × 1
Dump C	1234	ccam05232	13:32	1 × 5
Dump D	1234	ccam04232	13:26	1 × 5
Dwyka	1234	ccam07232	14:09	10 × 1
Presieve (Dump F)	1253	ccam01253	12:47	1 × 5
Postsieve (Dump E)	1253	ccam02253	12:54	1 × 5 (3 on target)
Garub	1167	mcam05284	11:56	---
Hoanib	1182	mcam05356	12:16	---
Kubib	1183	mcam05362	12:11	---
Dumps A and B	1229	mcam05651/5652	12:20	---
Hakos	1233	mcam05703	13:39	---
Dumps C and D	1234	mcam05707	13:03	---
Presieve and postsieve (Dumps E and F)	1253	mcam05852	13:13	---

## 2. Previous Observations of Dune Sands and/or Ripple Forms

### 2.1. Orbital Observations of Gale Crater Dunes

Initial studies of Gale Crater using orbital data noted the overall mafic nature of the Bagnold Dunes and that a variety of aeolian landforms existed, including barchans and longitudinal dunes [Milliken *et al.*, 2010; Anderson and Bell, 2010]. Thermal inertia values from Viking infrared thermal mapper observations were consistent with unconsolidated sand-sized grains [Edgett and Christensen, 1994]. Analyses of orbital Thermal Emission Spectrometer (TES) observations demonstrated that the Bagnold Dune area exhibits an olivine basalt composition [Rogers and Bandfield, 2009]. Lane and Christensen [2013] used TES data in combination with laboratory thermal emissivity spectra of synthetic olivines to predict an olivine composition for the Bagnold Dune area of  $\sim\text{Fo}_{55\pm 5}$ . Seelos *et al.* [2014] used Compact Reconnaissance Imaging Spectrometer for Mars (CRISM) data to demonstrate compositional differences between dune types, such that barchan dunes were more olivine rich compared to more high-calcium pyroxene associated with longitudinal dunes. They suggested that aeolian processes may preferentially winnow lower density pyroxene-rich materials and leave behind denser olivine grains within barchan dunes, although Ehlmann and Buz [2015] noted that additional study was needed to determine whether variations in olivine versus pyroxene resulted from source bedrock composition or from aeolian sorting. As summarized by Hobbs *et al.* [2010] and Silvestro *et al.* [2013], these migrating barchanoid duneforms amalgamate into longitudinal dunes along the edge of Mount Sharp as a result of two dominant wind directions from the northwest and northeast, although such regional north winds are greatly influenced by crater-scale secondary flow patterns [Day and Kocurek, 2016]. In their models of CRISM data (over the 800–2500 nm range) of the Bagnold area, Lapotre *et al.* [2017] also determined that the sands were mainly basaltic and showed distinct variations in composition, likely as a result of aeolian sorting.

### 2.2. In Situ Observations of Dark Sands

Although neither of the Viking Landers found dark soil deposits at their landing sites, Bell *et al.* [2000] examined dark soils using the Imager for Mars Pathfinder (IMP) multispectral camera and images from the Sojourner rover. Darker soil units exhibited negative 800 to 1000 nm spectral slopes. Undisturbed dark soils were characterized by lower red/blue reflectance ratios than rover-disturbed dark soils. The latter exhibited a weak 800–1000 nm absorption band. Dark soils were relatively coarse grained and/or mixed with dark ferrous materials relative to more ferric-rich bright soils (although the ferrous component was poorly constrained by IMP data). Nonetheless, Pathfinder alpha proton X-ray spectrometer data of soils showed

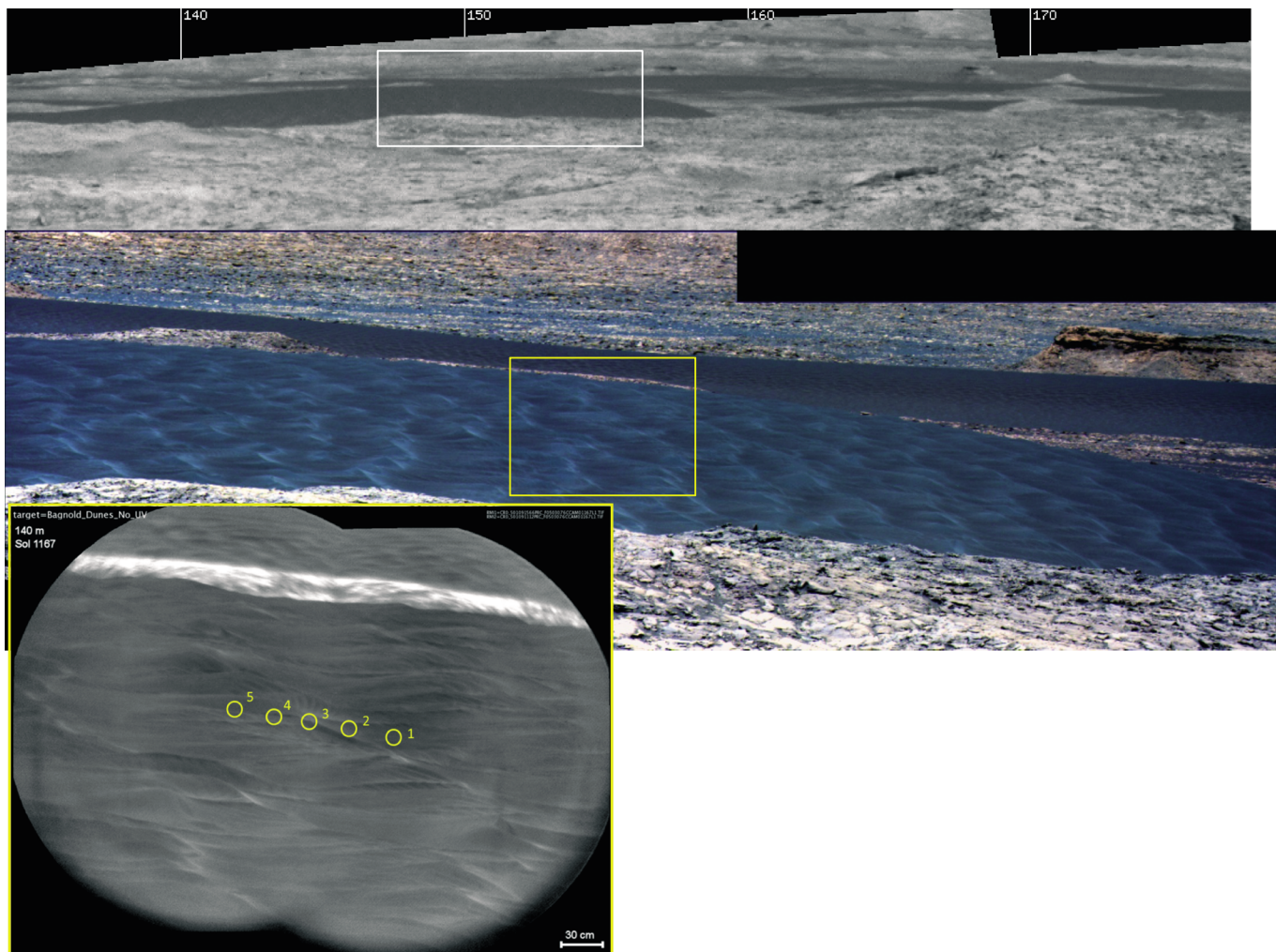


**Figure 2.** Location of long-distance (~140 m) ChemCam passive observation of Namib Dune acquired on Sol 1167. (top) Portion of Navcam mosaic from Sol 1162 (site 50, drive 3076; annotated with azimuth designations) looking toward southeast (compare to dash-dotted line in Figure 1). White box outlines region encompassed by enhanced false-color M100 camera mosaic (middle) acquired on Sol 1167 (portion of mcam05287). Yellow box approximates outline of RMI mosaic (bottom) showing five locations from which passive spectra were acquired (Figure 3). Circles approximate the ~9 cm field of view of each observation.

little variability and remarkable similarity to the average Viking-derived soil elemental compositions [cf. *Toulmin et al.*, 1977; *Clark et al.*, 1982; *Banin et al.*, 1992].

*McSween et al.* [2010] used Mössbauer data, Alpha Particle X-ray Spectrometer (APXS) data, and Miniature Thermal Emission Spectrometer (Mini-TES) thermal infrared spectra to suggest that the average dark soils at both Mars Exploration Rover (MER) sites represented a mixture of igneous minerals (olivine, pyroxene, plagioclase, Fe-Ti-Cr spinels, and phosphate) and alteration materials. The latter included amorphous silica, hematite, nanophase oxides, and clays, with S and Cl incorporated into either sulfate plus chloride or with schwertmannite and akaganeite. They interpreted this mixture to represent different sources for the igneous and alteration components, which experienced no appreciable in situ alteration. Because the ratio of these mixed components was essentially the same at the two MER sites, they suggested that Martian soils provided a representative sampling of the overall crustal mineralogy.

*Rogers and Aharonson* [2008] studied the mineralogy of low-albedo sands at Meridiani Planum using Opportunity rover Mini-TES, Mössbauer, and APXS data to show that the sands were olivine basaltic with minor sulfate and a high-silica phase (glass or secondary amorphous silica). Their models suggested that olivine abundance (10–15%) was about half that of low-calcium pyroxene. Model results from orbital measurements using data from TES were within 5% of those derived from MER data. For comparison,

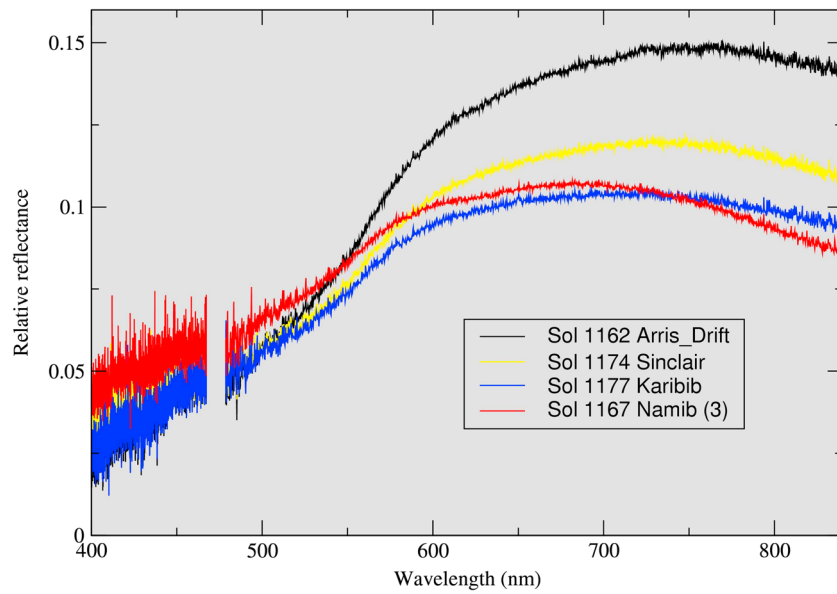


**Figure 3.** ChemCam passive spectra of three soil locations north of Bagnold Dunes compared to long-distance observations of Namib Dune (location #3 in Figure 2). The development of a weak absorption band near 620 nm and peak reflectance position near 685 nm followed by steep downturn are consistent with olivine in the dune sands. Gap between 468 and 478 nm represents region between ChemCam detectors.

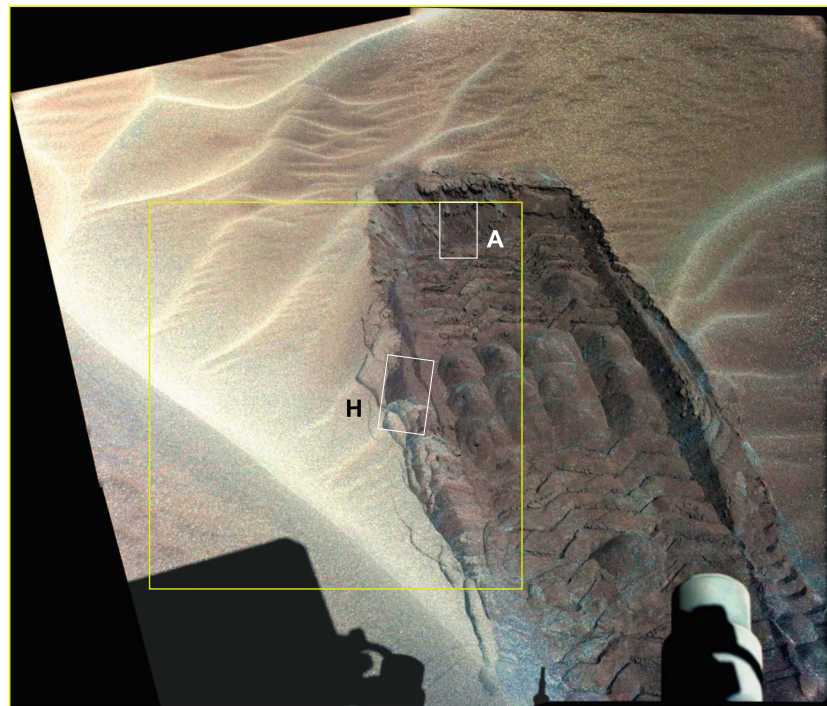


**Figure 4.** Mastcam M34 enhanced color mosaic (Sol 1181, mcam05350) acquired in the High Dune area showing location of Hoanib (H) and Awasib (A) ChemCam targets (RMI mosaics outlined in small boxes; see Figures 6 and 7); large box outlines M34 coverage from Mastcam multispectral frame (Figure 5). Maximum width of wheel track disturbed area is ~60 cm.

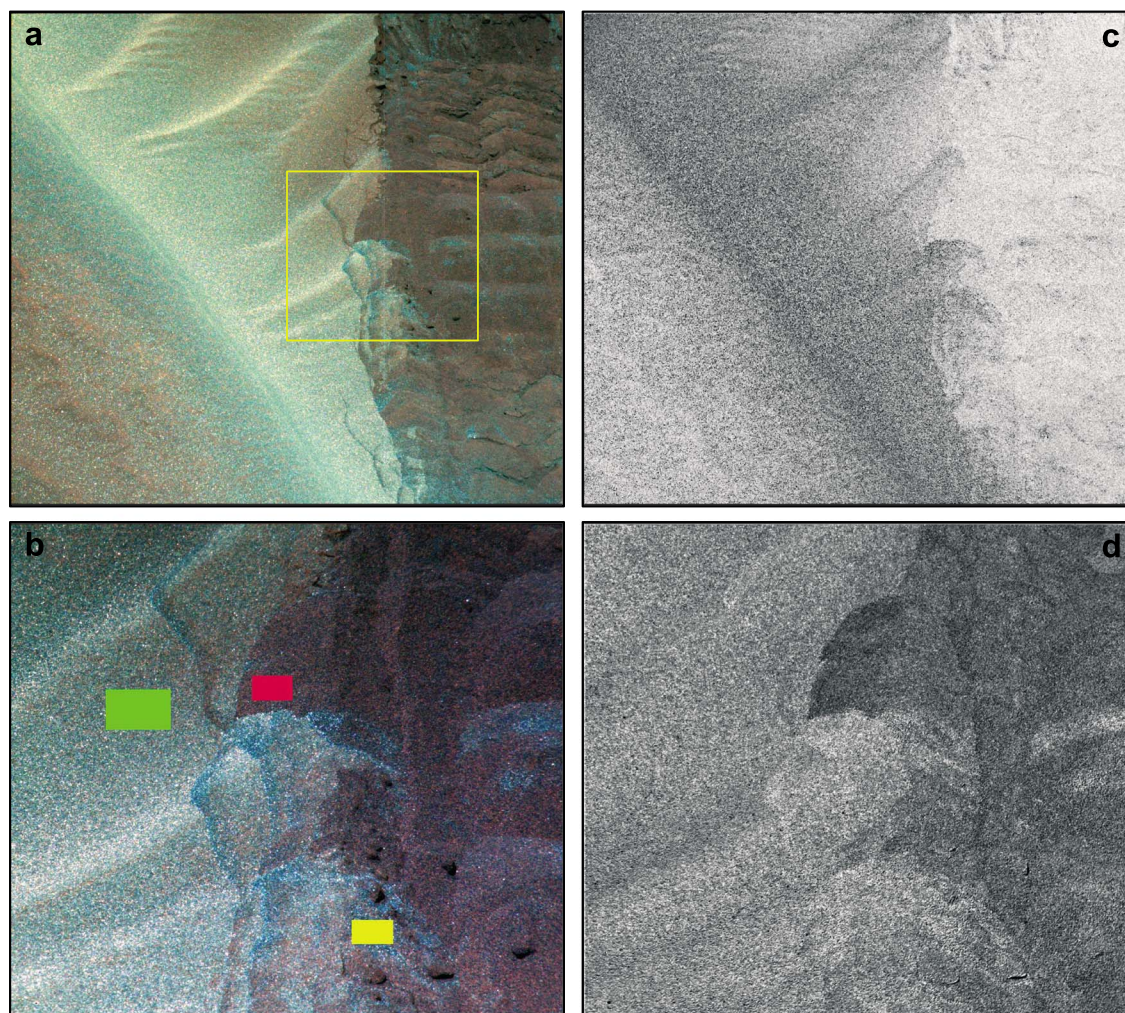


**Figure 5.** (a) Mastcam M34 false-color image (751, 527, and 445 nm) of Hoanib area disturbed and undisturbed sands in High Dune (Sol 1182, mcam05356); yellow box shows location of M100 coverage shown in Figure 5b, which is a false-color image (805, 527, and 447 nm). (b) colored boxes represent regions of interest from which Mastcam spectra were extracted (see Figure 9; red = disturbed soil; green = undisturbed sand; yellow = disturbed sand). (c) 527 nm band depth map for M34 area (brighter tones represent stronger band depths). (d) 638/1013 nm ratio map (using red Bayer filter and 1013 nm (R6) filter) for M100 area (darker tones represent areas where relative reflectance at 1013 nm is greater than that at 638 nm).

*Morris et al.* [2006] used Mössbauer data to show that typical basaltic sands at Meridiani had low  $\text{Fe}^{3+}/\text{Fe}_{\text{Total}}$  ratios (0.2–0.4), with average proportions of total iron noted for the following basaltic minerals: olivine (33%), pyroxene (38%), nanophase oxide (18%), magnetite (6%), and hematite (4%).

Along the MER Spirit rover's traverse, El Dorado was a well-investigated, low-albedo area with sand ripples. *Sullivan et al.* [2008] used Pancam multispectral data to show that the relatively dust free 200–300  $\mu\text{m}$  sands were bluer in visual wavelengths and had negative 673–1009 nm spectral slopes, similar to laboratory spectra of olivine grains coarser than  $\sim 60 \mu\text{m}$  [cf. *King and Ridley*, 1987]. Finer-grained materials ( $\leq 100 \mu\text{m}$ ) were redder and exhibited a slightly positive 934–1009 nm spectral slope, consistent with the presence of more low-calcium pyroxene. This resulted in coarser sands appearing “bluer” or less “purple” than finer sands in stretched, false-color Pancam images. The apparent correlations between color, grain size, and composition were observed only where wind had sorted and segregated the particles into resolvable deposits that were less contaminated with air fall dust. *Sullivan et al.* [2008] speculated that this correlation might have derived from a single original basalt composition. They also reasoned that because olivine and quartz are similar in hardness and conchoidal fracturing patterns compared to pyroxenes (which more easily fracture along cleavage planes), ongoing aeolian processing of lithic fragments from a basaltic precursor could result in a coarser population of olivine-rich particles forming as a lag deposit. Indeed, *Morris et al.* [2008] determined

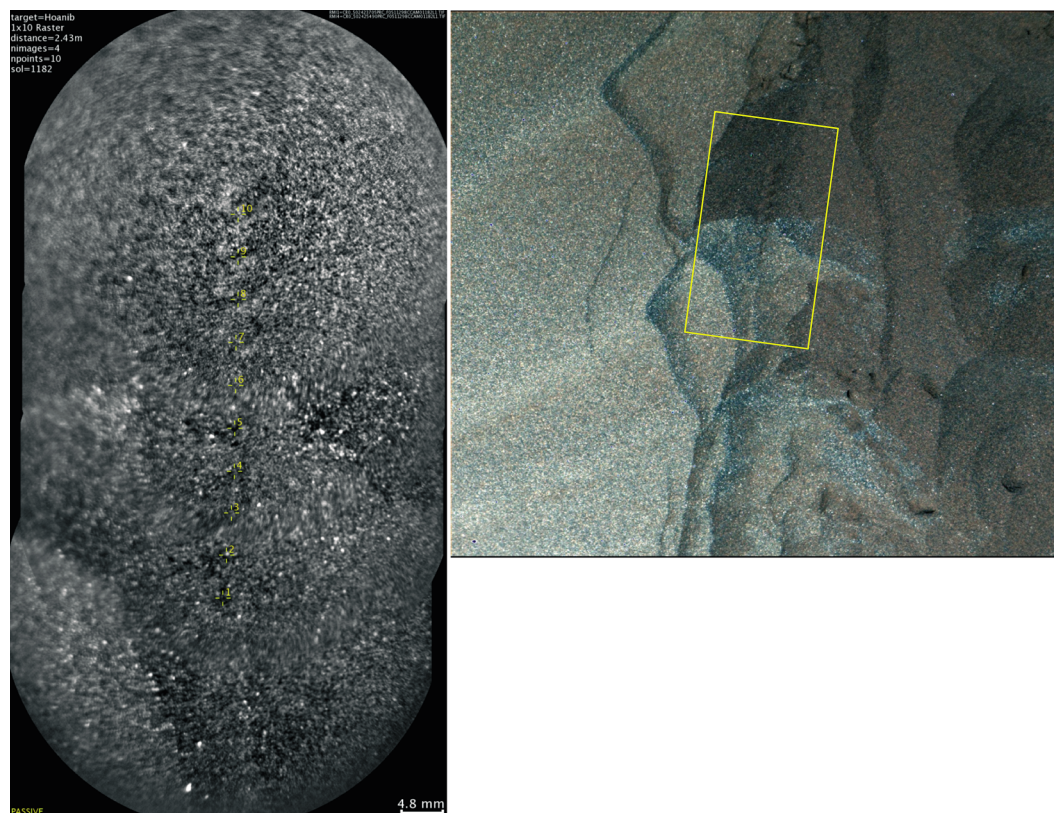


**Figure 6.** RMI mosaic of Hoanib (Sol 1182; ccam01182) showing 10 numbered locations of ChemCam observations and post-LIBS Mastcam M100 enhanced color image (Sol 1182, mcam05359); yellow box approximates extent of RMI mosaic.

through Mössbauer data that although a scuffed region in El Dorado was somewhat similar to Spirit basaltic soils, it had a higher proportion of Fe from olivine (47%) and corresponding lower proportions of Fe from pyroxene (32%) and especially nanophase oxide (8%). We undertook an analysis of Mini-TES data of El Dorado (not shown) to evaluate the composition of the olivine in El Dorado dune and found  $\sim 15\%$  olivine ( $\sim \text{Fo}_{40 \pm 10}$ ), along with  $\sim 37\%$  amorphous material, and  $\sim 22\%$  Mg and Fe sulfates.

Along the MSL traverse, the Rocknest aeolian deposit was somewhat similar to landforms observed by the MER rovers, although not as low albedo as El Dorado. *Blake et al.* [2013] found that the  $<150 \mu\text{m}$  fraction contained  $\sim 55\%$  crystalline material consistent with a basaltic protolith (28.5 wt % pyroxene, 22.4 wt % olivine ( $\text{Fo}_{61 \pm 3}$ ), and 40.8 wt % plagioclase) and  $\sim 45\%$  X-ray amorphous material that was iron rich. The Rocknest  $\sim 12$  wt % bulk olivine abundance was among the largest observed in ChemMin observations prior to Bagnold Dunes. For example, Yellowknife Bay mudstones contained 2–4 wt % olivine [*Vaniman et al.*, 2014] and the Windjana sample  $\sim 6$  wt % [*Treiman et al.*, 2016]. This is consistent with the relative lack of olivine in bedrock at Gale Crater as interpreted from overall low (Mg + Fe)/Si ratios in ChemCam laser-induced breakdown spectroscopy (LIBS) data [e.g., *Sautter et al.*, 2016], although orbital observations demonstrate extensive olivine in the walls of Gale Crater [*Ehlmann and Buz*, 2015]. The relative paucity of olivine at Yellowknife Bay also has been interpreted to result from alteration of Mg saponite [*Vaniman et al.*, 2014; *Bristow et al.*, 2015]. For comparison, TES global analyses indicate that olivine-bearing materials typically contain  $\sim 5$ –20% olivine [*Koepfen and Hamilton*, 2008; *Rogers and Hamilton*, 2015; *Hanna et al.*, 2016].

### 3. Data Sets Acquired

The primary ChemCam and Mastcam data sets used here and their observation sequence identifications are listed in Table 1. In the discussions below, we typically refer to “sand” as dominantly coarse-grained surface materials and “soil” as materials that are a combination of coarse- and fine-grained materials (including dust and/or subsurface grains). ChemCam measurements were acquired as the rover approached Bagnold Dunes



**Figure 7.** RMI mosaic of Awasib (Sol 1182; ccam02182) showing five numbered locations of ChemCam observations and post-LIBS Mastcam M100 enhanced color image (Sol 1182, mcam05358); yellow box approximates extent of RMI mosaic.

(Figure 1), with the intent of monitoring the contribution of dune sands to nearby areas. These observations began with Arris\_Drift (Sol 1162) and included the sand targets Sinclair (Sol 1174) and Karibib (Sol 1177) on the eastern edge of High Dune. On Sol 1167, ChemCam was able to view a portion of Namib Dune from 140 m distance (Figure 2). At the same location, Mastcam multispectral observations were acquired of undisturbed soils at Garub on Sol 1167. Once Curiosity was stationed on the eastern edge of High Dune to conduct rover engineering tests, ChemCam observations of undisturbed and disturbed areas at the targets Hoanib and Awasib (Sol 1182) were made, and Mastcam multispectral images were acquired of Hoanib (Sol 1182) and the disturbed area Kubib (Sol 1183). On Sol 1184 ChemCam measurements were acquired of a nearby ripple crest (Barby) and trough (Kibnas). Once at the western edge of Namib Dune, the area referred to as Gobabeb was the site of sieving tests for Dump samples A ( $<150\ \mu\text{m}$ ), B ( $>150\ \mu\text{m}$ ), C ( $150\text{--}1000\ \mu\text{m}$ ), and D ( $>1000\ \mu\text{m}$ ). Dump D was suggested to contain few particles  $>1000\ \mu\text{m}$  by *Ehlmann et al.* [2017]. A nearby typical, undisturbed small ripple crest (Dwyka) was also observed for context on Sol 1234. Mastcam multispectral images were acquired of Dumps A and B (Sol 1229), C and D (Sol 1234), and the nearby rover track at Hakos (Sol 1233). After the rover drove back to the eastern edge of High Dune, the presieved and postsieved samples from the third scoop (grain size fractions of  $>150\ \mu\text{m}$  (Dump F) and  $<150\ \mu\text{m}$  (Dump E), respectively) were dumped and analyzed on Sol 1253 by both ChemCam and Mastcam.

## 4. Methodology

### 4.1. ChemCam Passive Spectra

The laser-induced breakdown spectroscopy (LIBS) portion of the ChemCam instrument disperses light emitted from a laser-generated plasma onto three spectrometers to detect elemental emission lines at high spectral ( $<1\ \text{nm}$ ) and spatial ( $0.65\ \text{mrad}$  field of view (FOV)) resolution [Wiens *et al.*, 2013, 2015]. Johnson *et al.* [2015a, 2016] demonstrated that the ChemCam “violet” (VIO, 382–469 nm) and visible/near-infrared (VNIR, 474–906 nm) spectrometers exhibited sufficient sensitivity to allow collection of useful surface spectral

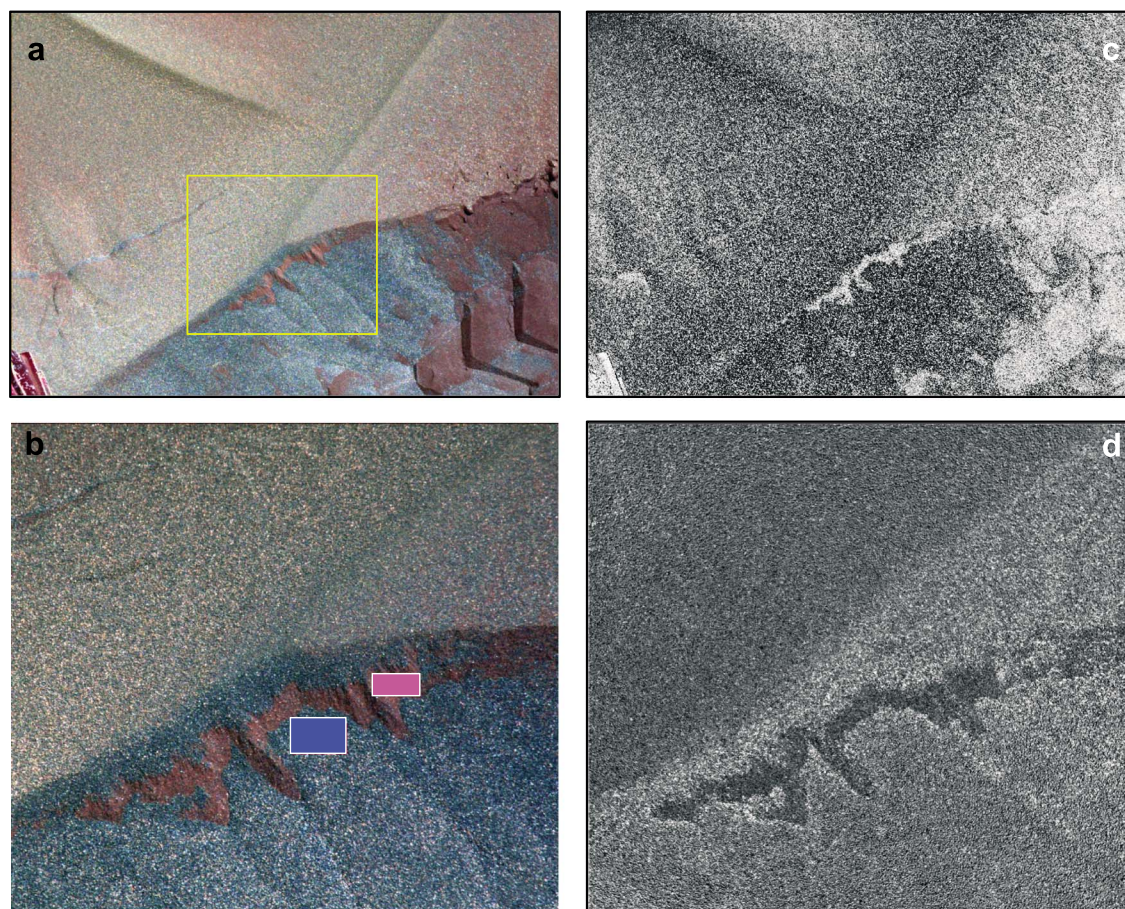


**Figure 8.** (a) Mastcam M34 false-color image (751, 527, and 445 nm) of Kubib area disturbed and undisturbed sands in High Dune (Sol 1183, mcam05362); yellow box shows location of M100 coverage shown in Figure 8b which is a false-color image (805, 527, and 447 nm) and covers a region ~25 cm across. (b) colored boxes represent regions of interest from which Mastcam spectra were extracted (see Figure 9; blue = sand; magenta = soil). (c) 527 nm band depth map for M34 area (brighter tones represent stronger band depths). (d) 638/1013 nm ratio map (using red Bayer filter and 1013 nm (R6) filter) for M100 area (darker tones represent areas where relative reflectance at 1013 nm is greater than that at 638 nm).

reflectance in passive mode (i.e., without using the laser). In the following we refer to these spectra as “ChemCam passive spectra” (or simply as “ChemCam spectra”). *Johnson et al.* [2015a] presented relative reflectance spectra (400–840 nm) of rocks, dust, and soils near the rover (~2–7 m) where spatial resolutions of the point locations ranged from 1.3 to 4.5 mm. Analyses of the band depths, spectral slopes, and ratios among these spectra revealed spectral end-members characterized by variations in ferrous and ferric components. These included brushed or freshly broken surfaces (“exposed” materials) with low 535 nm band depths and low 670/440 nm ratios, indicative of the less oxidized nature of these more ferrous materials relative to the typical reddish, dusty surfaces found on undisturbed rocks and soils. “Dark” float rocks exhibited low relative reflectance and significant downturns longward of 700 nm that were consistent with the presence of low-Ca pyroxene.

For every LIBS point measurement acquired by ChemCam with its laser, a 3 msec exposure passive (dark) measurement was acquired without the laser for the purpose of subtracting the ambient light from the LIBS spectrum. Longer exposure passive measurements at 30 msec were acquired for specific targets of interest when possible to increase the signal-to-noise ratio. We converted the raw data to radiance using the methods described by *Johnson et al.* [2015a]. The ratio of a scene radiance to that of the white ChemCam calibration target holder radiance (measured on Sol 76 at the same exposure time to minimize dark current differences) was multiplied by the known laboratory reflectance of the calibration target material [*Wiens et al.*, 2012] to provide an estimate of relative reflectance. *Johnson et al.* [2015a] estimated that the radiance absolute calibration uncertainty was 6–8%, sufficient to characterize band positions and shapes useful in constraining

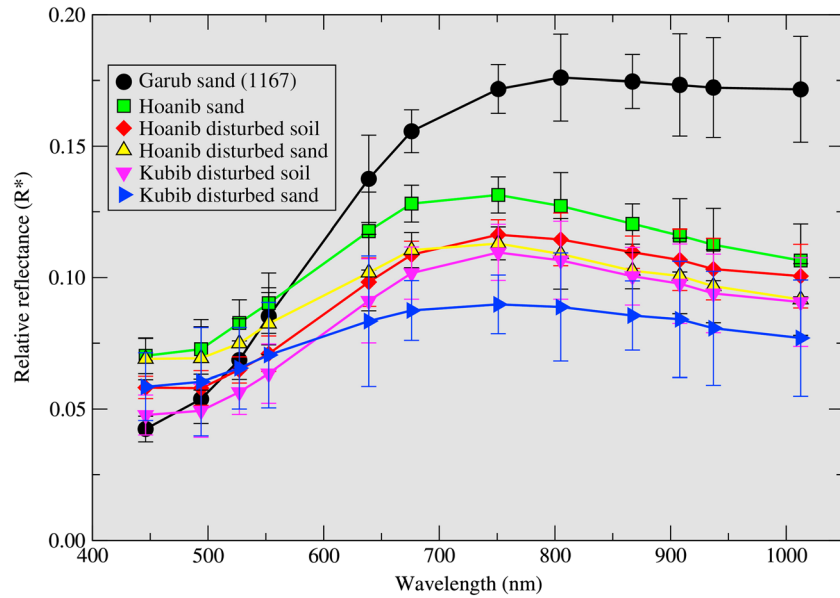


**Figure 9.** Mastcam spectra of Hoanib (mcam05356) and Kubib (mcam05362) targets (ROI locations shown in Figures 5 and 8, respectively, color coded to spectra color). Garub sand (from Sol 1167, mcam05284) is a typical Gale sandy area encountered prior to entering the Bagnold Dune area. Error bars represent standard deviations within selected region of interest. Garub data acquired at ~11:58 Local True Solar Time (LTST) at phase angle ~39°, Hoanib data at ~12:16 LTST at phase angle ~74°, and Kubib data at ~12:12 LTST at phase angle 36°.

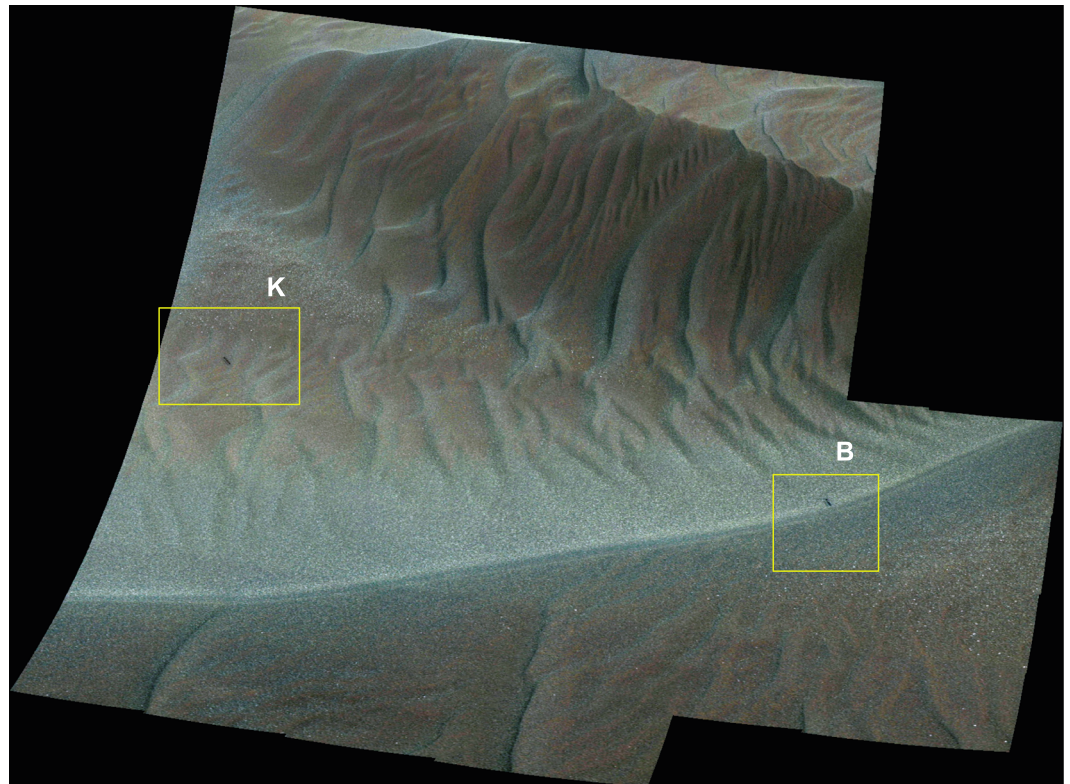


**Figure 10.** Enhanced color Mastcam M100 mosaic (Sol 1184 mcam05372) showing Barby (B; ripple crest) and Kibnas (K; ripple trough) ChemCam observations in the High Dune area. Yellow boxes outline regions of Mastcam M100 images shown in Figures 11 and 12.

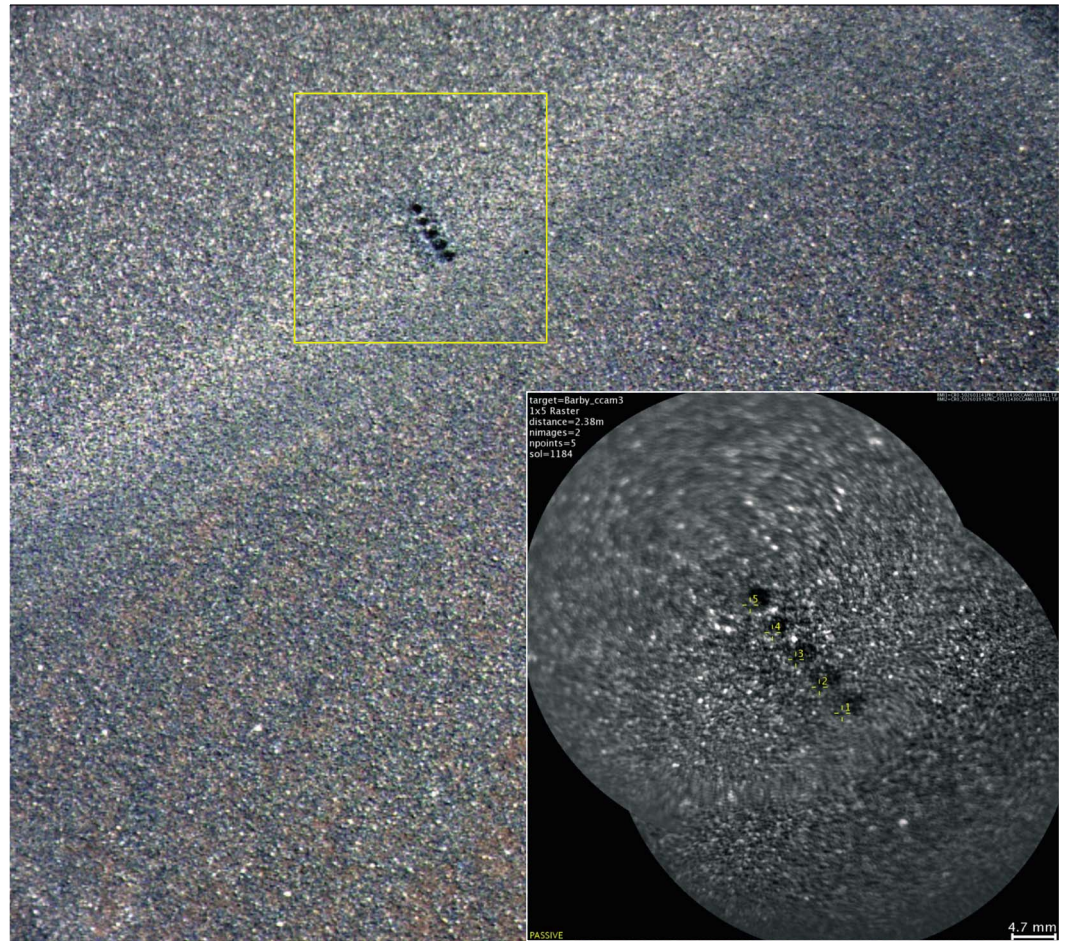


**Figure 11.** Enhanced color Mastcam M100 image (Sol 1184, mcam05372) of Barby target ripple crest, with RMI mosaic inset (Sol 1184, ccam01184) showing numbered ChemCam raster locations.

compositions and/or mineral detections. The 0.65 mrad FOV of the instrument corresponds to an  $\sim 2$  mm spot size at an observation distance of 3 m. Longer-distance observations' effective FOVs are subject to minor, variable elongation resulting from the projection of the FOV onto local topography (cf. Figure 2).

Remote Micro-Imager (RMI) images were acquired as part of ChemCam observations, from which accurate locations for the individual points within a raster could be placed [Wiens *et al.*, 2012, 2015; Maurice *et al.*, 2012, 2016; Le Mouélic *et al.*, 2015]. Comparison to Mastcam images acquired as part of the ChemCam observations also provided context images for interpreting the passive spectra. However, direct comparison is limited owing to the broadband nature of the RMI band pass, whose maximum responsivity is near 700 nm. For comparison, the standard Mastcam Bayer filters are centered near 495, 554, and 640 nm [Wellington *et al.*, 2016].

Analyses of ChemCam spectra benefited from the use of spectral parameters calculated using  $\pm 5$  nm averages around a central wavelength. In the visible wavelengths, 600/440 nm ratios are sensitive to oxidation state and/or dust deposition, whereas red/near-infrared ratios (700/840 nm and 600/700 nm) are indicative of the strength of iron absorptions from mafic minerals. The 535 nm band depth is sensitive to the presence of crystalline ferric oxides [e.g., Morris *et al.*, 1997, 2000] and was calculated with a continuum between 500 nm and 600 nm [cf. Bell *et al.*, 2000]. The peak reflectance values were also used to investigate correlations with other parameters.

#### 4.2. Mastcam Spectra

Mastcam comprises two  $1600 \times 1200$  pixel Bayer-patterned CCD cameras located on the rover's remote sensing mast  $\sim 2$  m above the surface. A radiometric calibration target is mounted on the rover deck below

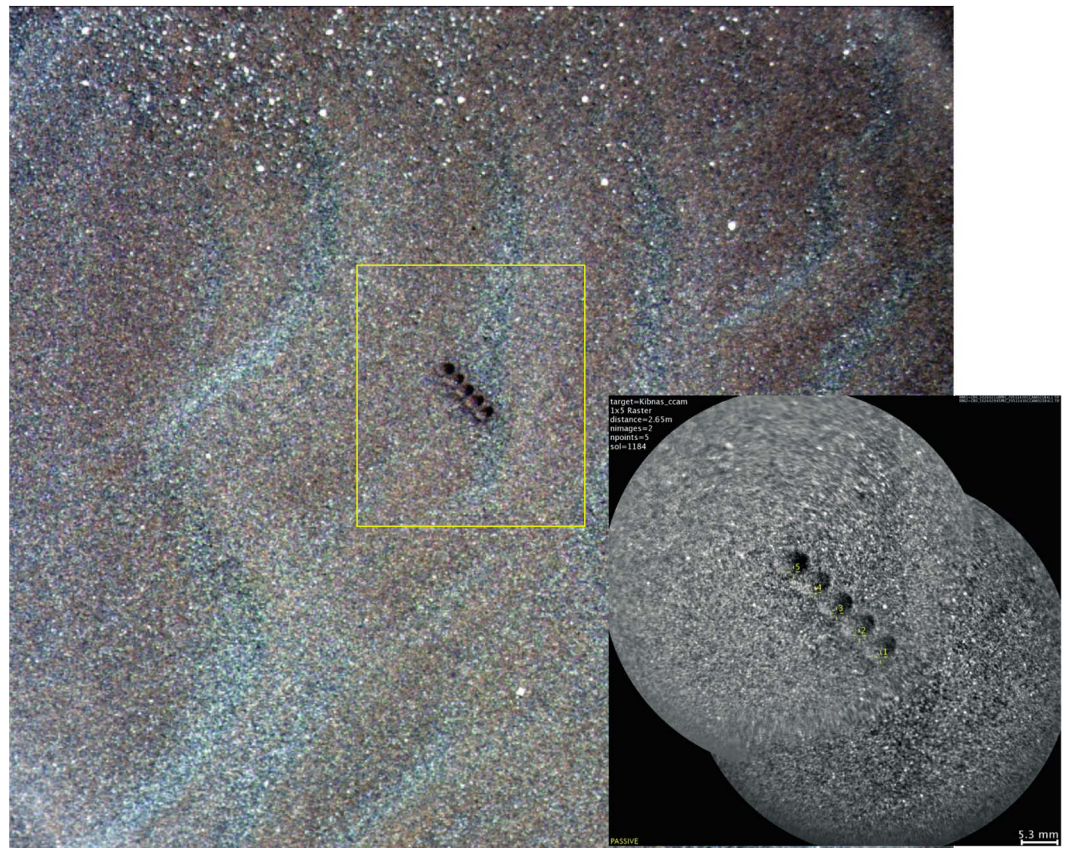


**Figure 12.** Enhanced color Mastcam M100 image (Sol 1184, mcam05373) of Kibnas target (ripple trough), with RMI mosaic inset (Sol 1184, ccam02184) showing numbered ChemCam raster locations.

the ChemCam calibration target. The Mastcam right camera (M100, 100 mm focal length) obtains spatial resolution about 3 times better compared to the left camera (M34, 34 mm focal length). Each camera includes an eight-position filter wheel with narrow band filters selected to characterize the visible to near-infrared reflectance spectra of targets in the wavelength range of 445–1013 nm. One position on each filter wheel is occupied by a broadband infrared-cutoff filter for RGB color imaging that makes use of a  $2 \times 2$  unit cell Bayer pattern bonded directly to the detectors [Wellington *et al.*, 2016]. The combination of filters between the two cameras provides 12 center wavelengths for multispectral analysis, including the three RGB Bayer bands.

Preflight calibration measurements were used to convert raw Mastcam data to radiance ( $W/m^2/nm/sr$ ) using the techniques described by Wellington *et al.* [2016] and Bell *et al.* [2003]. Conversion to radiance factor ( $I/F$ , where  $I$  is the measured scene radiance and  $\pi F$  is the solar irradiance at the top of the Martian atmosphere) incorporated near-real-time observations of the onboard Mastcam calibration target, corrected for illumination and viewing geometry by means of a modified He-Torrance model [He *et al.*, 1991; Bell *et al.*, 2003] and corrected for dust deposition [Kinch *et al.*, 2015; Wellington *et al.*, 2016]. Observations calibrated to radiance factor were divided by the cosine of the solar incidence angle to generate relative reflectance ( $R^*$ ), an approximation of the reflectance factor defined in Hapke [1993, 2012]. Relative reflectance spectra are presented as the average values derived from manually defined regions of interest (ROIs) selected to represent the same region in the M34 and M100 cameras. Error bars in spectral plots represent the standard deviation of the selected pixels within each ROI. Right-eye filter values are scaled to the left-eye values at the longest wavelength (1013 nm, which is least affected by uncertainties in the dust correction) and averaged with the left-eye values at overlapping wavelengths to produce one combined spectrum. The absolute radiometric accuracy for Mastcam has been estimated at 10–20%, with a filter-to-filter uncertainty of  $<5\%$  and pixel-to-pixel variation of  $<1\%$  [Bell *et al.*, 2003, 2013; Wellington *et al.*, 2016].

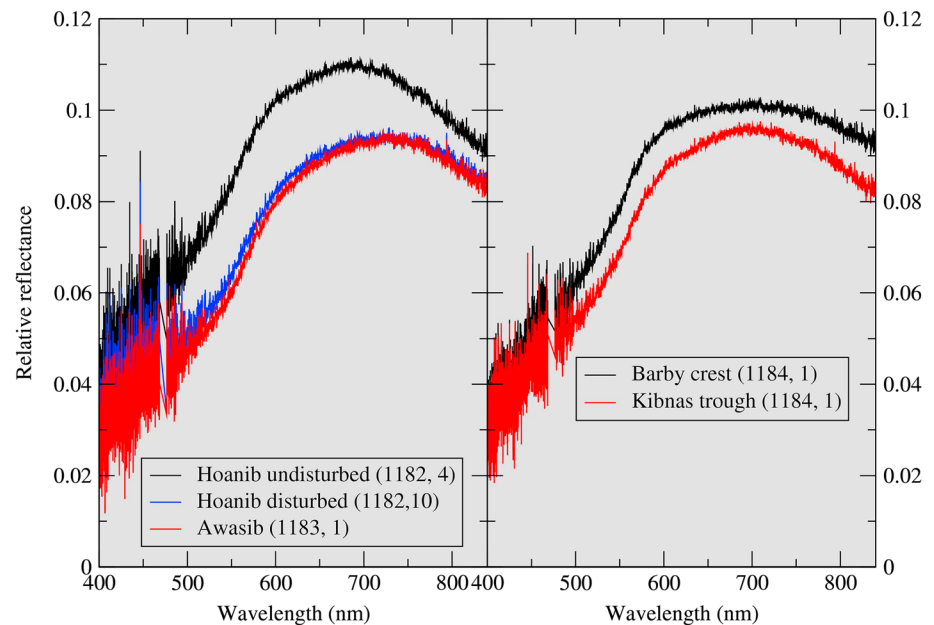


**Figure 13.** ChemCam passive spectra of High Dune areas Hoanib and Awasib (Figures 4–7) and ripple crest (Barby) and trough (Kibnas) (Figures 10–12). Sol number and location number with ChemCam raster are shown in parentheses. All spectra acquired prior to LIBS laser shot at that location. Gap between 468 and 478 nm represents region between ChemCam detectors.

Spectral parameters were also calculated from Mastcam spectra to assist with analysis, using wavelengths similar to the ChemCam spectral parameters. These included parameters sensitive to ferric crystallinity, oxidation state, and/or dust deposition, such as the band depth at 527 nm, the peak reflectance value, 639/446 nm ratio, and the visible spectra slope between 446 nm and 639 nm. Red/near-infrared parameters more sensitive to mafic minerals included the 676/751 nm ratio and the 676/876 nm ratio.

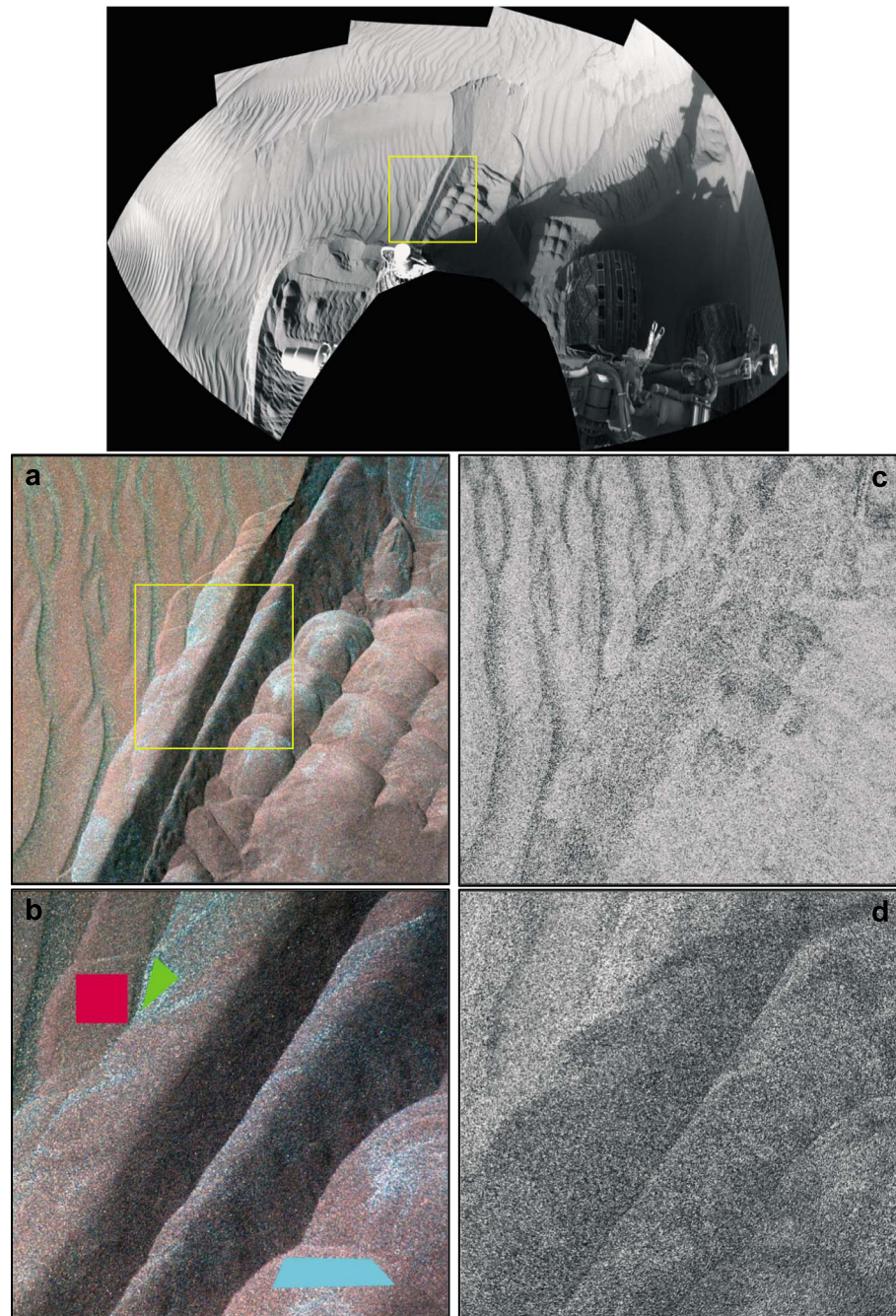
## 5. Results

### 5.1. North of Bagnold Dunes

ChemCam spectra of three locations north of Bagnold Dunes are compared in Figure 3 to the spectrum of Namib Dune acquired from ~140 m distance. The Arris\_Drift target represents a typical dusty soil spectrum, albeit with lower peak relative reflectance (0.15) and minor near-infrared downturn, indicative of some component similar to Bagnold Dune sands. This is consistent with orbital observations showing small pockets of dark-toned materials scattered around the main perimeter of Bagnold Dunes, particularly in topographic lows, which likely contribute some small proportion of sand-sized grains. This is emphasized by the decreasing reflectance and greater near-infrared downturns observed at the less dusty Sinclair and Karibib sand locations that are closer to High Dune. For comparison, the long-distance Namib Dune spectrum shows the steepest near-infrared downturn, which begins near 685 nm compared to longer wavelengths for the other spectra. The Namib spectrum also exhibits greater relative reflectance below 500 nm, a weaker 535 nm band, and a weak absorption band near 620 nm (manifested by the relatively flat spectral slope in the 600–700 nm region). These spectral features are all consistent with olivine-bearing materials in the Namib spectrum, likely with some contribution from pyroxene within the ~9 cm field of view for each spectrum. Furthermore, the Namib spectrum was acquired at a 120° phase angle (midday solar incidence angle but horizon-level emission angle). Given the forward scattering nature of dune sands on Mars [Geissler and Singer, 1992; Johnson *et al.*, 2015b], this geometry could cause some phase reddening [e.g., Pommerol *et al.*, 2013; Schröder *et al.*, 2014] compared to the other spectra, which were acquired under less extreme phase angles.

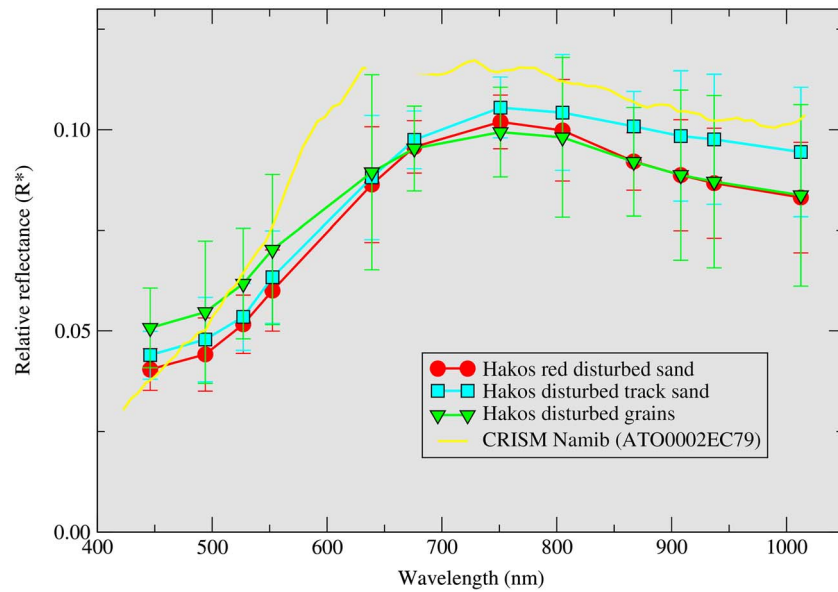
### 5.2. High Dune Area

Figure 4 shows an enhanced M34 color mosaic of the rover wheel track made at a sand patch near High Dune in which the targets Hoanib and Awasib were selected to sample both the disturbed and undisturbed



**Figure 14.** (top) Navcam mosaic from Sol 1221 (ncam0352) showing location of (a) Mastcam M34 false-color image (751, 527, and 445 nm) of Hakos area disturbed and undisturbed sands in the Namib Dune area (Sol 1233, mcam05703); box shows location of (b) M100 frame, which is false-color image (805, 527, and 447 nm) and covers a region ~25 cm across; colored polygons represent regions of interest from which Mastcam spectra were extracted (see Figure 15; red = disturbed sand; green = disturbed grains; cyan = disturbed track sand). (c) 527 nm band depth map for M34 area (brighter tones represent stronger band depths). (d) 638/1013 nm ratio map (using red Bayer filter and 1013 nm (R6) filter) for M100 areas (darker tones represent areas where relative reflectance at 1013 nm is greater than that at 638 nm).

portions of the ripple area. Figure 5a shows a false-color M34 image of the Hoanib target, and Figure 5b shows a false-color M100 image superimposed with ROIs selected for Mastcam spectra on the reddish disturbed soil (red ROI), bluer disturbed sand (yellow), and undisturbed sand (green). Figure 5c shows the 527 nm band depth image for the M34 area in which brighter tones observed in the disturbed material



**Figure 15.** Mastcam spectra of Hakos area at Namib Dune. Locations are shown in Figure 14. Error bars represent standard deviations within selected region of interest. CRISM spectrum is from sequence ATO0002EC79 acquired over Namib Dune. Data were modeled as single-scattering albedo spectra with removal of gases and aerosols after modeling spatial and spectra transfer functions [Kreisch et al., 2016]. The single-scattering albedo spectrum was converted to  $R^*$  using equation 10.5 of Hapke [2012] (see text). Data from 637 to 690 nm are missing owing to the use of a fixed mounted filter on the CRISM detector that blocks higher orders from the grating [Murchie et al., 2007]. Data acquired ~13:40 LTST at phase angle ~56°.

represent stronger band depths (more ferric-rich materials). Figure 5d shows the 638/1013 nm ratio map for the M100 area, where darker tones represent areas where relative reflectance at 1013 nm is greater than that at 638 nm, consistent with less ferrous materials. Overall, the disturbed sands in the sand patch near High Dune exhibit spectral features indicative of more ferric components compared to the undisturbed surface sands. Additionally, undisturbed ripple troughs have more ferric components than ripple crests. Figures 6 and 7 show RMI mosaics of the Hoanib and Awasib targets, respectively, along with enhanced M100 images acquired under different lighting conditions than Figure 5.

Figure 8a shows a false-color M34 image of the Kubib area, which reveals materials disturbed by a wheel trenching activity. ROIs for Mastcam spectra are shown in the M100 false-color image (Figure 8b) for reddish, disturbed soil (magenta ROI) and disturbed sands (blue). The 527 nm band depth map for the M34 area (Figure 8c) exhibits lighter tones (stronger 527 nm band depths) in the redder, more ferric portions of the disturbed soils, including the region exposed directly below the surface. The M100 638/1013 nm ratio map

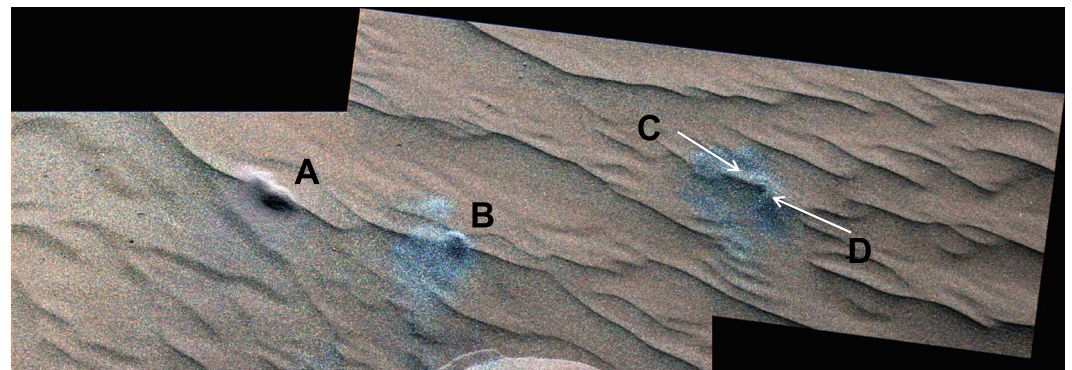


**Figure 16.** Enhanced Mastcam M34 mosaic (combined Sol 1226 mcam05614 and Sol 1230 mcam05700) of four sieved samples at Gobabeb Dune: A (<150  $\mu$ m), B (>150  $\mu$ m), C (150–1000  $\mu$ m), and D (>1000  $\mu$ m). Image width is ~1 m.

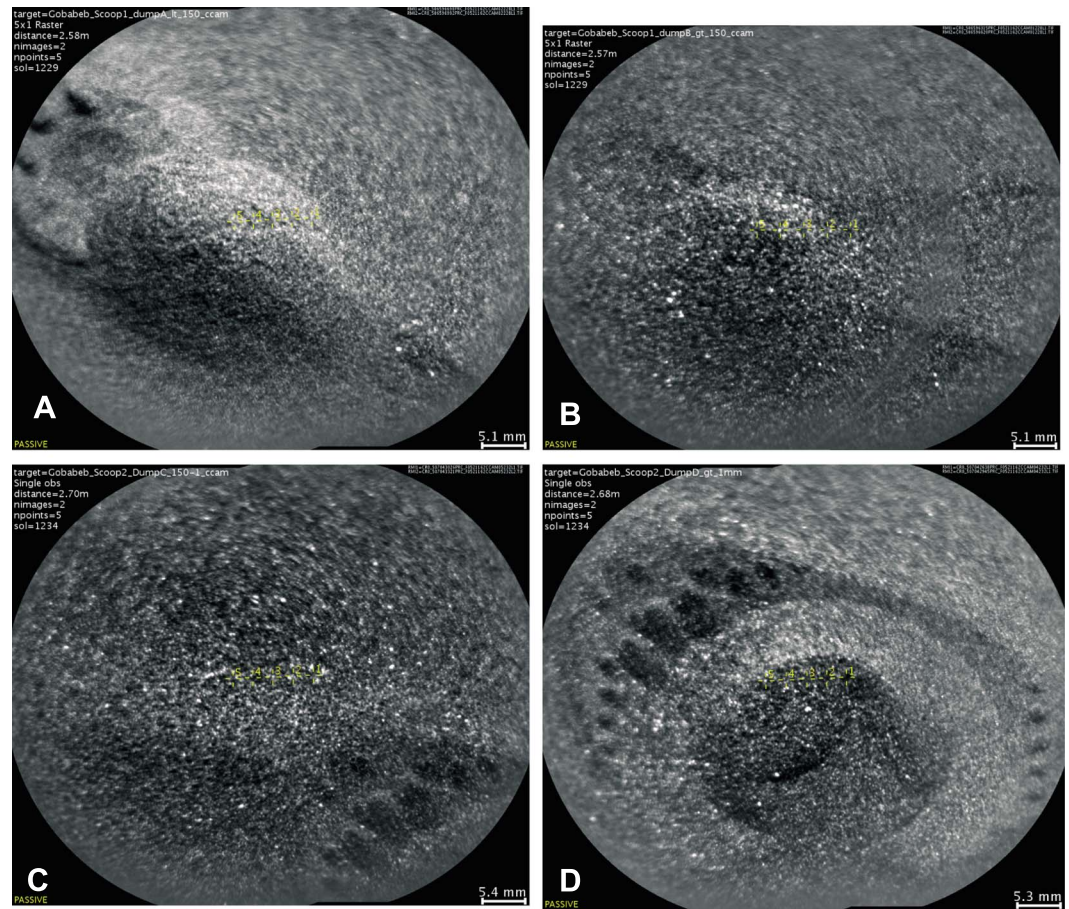


**Figure 17.** RMI image mosaics of four sieved sand piles A–D showing numbered ChemCam raster locations. Dump D was imaged after the APXS had touched the surface but prior to the LIBS observation that occurred later on Sol 1234.

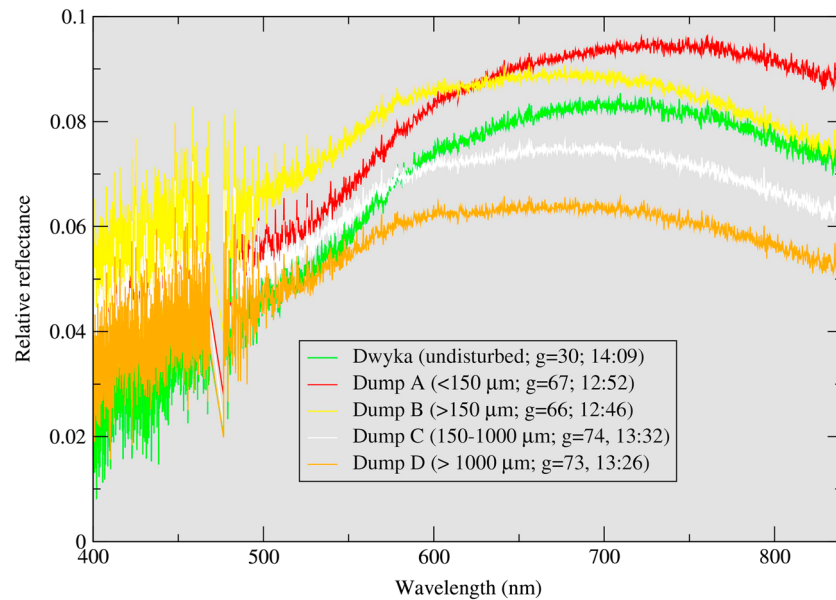
(Figure 8d) shows more positive red/near-infrared slopes (lower ratios) in these redder areas indicative of fewer ferrous components.

Figure 9 combines Mastcam spectra for the Hoanib and Kubib targets (color coded to their ROIs in Figures 5b and 8b), plus a spectrum of the Garub sandy area north of the Bagnold Dunes. All High Dune sands exhibit similar near-infrared downturns longward of 700 nm, with the Kubib sands exhibiting the darkest and flattest spectrum. The redder, disturbed, and exposed soils exhibit the lowest visible relative reflectance values, consistent with their greater 527 nm band depths.

Figure 10 shows an enhanced color M100 mosaic that identifies the ripple trough target Kibnas and the ripple crest target Barby for which ChemCam spectra were acquired. RMI mosaics and accompanying enhanced color M100 images of these areas are shown in Figures 11 and 12, in which it can be observed that the Barby area is on the lighter-toned side of a ripple crest, and the Kibnas area encompasses both redder and bluer areas within the rippled trough. Figure 13 compares the ChemCam spectra from representative raster locations acquired in the sand patches adjacent to High Dune (all of which were acquired prior to the corresponding LIBS shot). The Kibnas trough and Awasib and Hoanib disturbed soils all have similar spectra, with near-infrared downturns occurring longward of the peak reflectance near 700 nm. The Hoanib undisturbed sand exhibits a higher relative reflectance with the peak reflectance near 685 nm, and the near-infrared downturn is somewhat steeper. The Barby crest spectrum exhibits a flat spectral slope between ~600 and 750 nm followed by a similar downturn to Kibnas.

### 5.3. Namib Dune and Gobabeb Site

Figures 14a and 14b show false-color M34 and M100 images of the Hakos trench area on Namib Dune, with ROIs from which Mastcam spectra were extracted for partially disturbed sand (red ROI), brighter disturbed,



**Figure 18.** ChemCam passive spectra of four sieved piles from Gobabeb plus an undisturbed soil spectrum (Dwyka, Sol 1234, ccam07232). All spectra represent third location within a given raster; Dumps A–D were 30 msec exposures; Dwyka was a 3 msec exposure. Legend shows grain size range in each dump pile, as well as phase angle ( $g$ ) and LTST times for each observation.

sand-sized grains (green), and disturbed sand in the rover tracks (cyan). The 527 nm band depth map computed from M34 images is shown in Figure 14c, where the darker-toned areas correlate with bluer regions representative of collections of sand grains in the disturbed areas along the lee side of small ripples on the undisturbed surface. In the 638/1013 nm ratio map for M100 areas (Figure 14d) the disturbed areas are slightly darker, indicative of less negative near-infrared spectral slopes.

Figure 15 shows the Mastcam spectra for the Hakos disturbed materials, which exhibit minor variations related to the proportions of bluer disturbed sand grains (brightest in visible wavelengths) versus redder disturbed sands. Also shown in Figure 15 is an along-track oversampled CRISM spectrum of the Namib Dune area from *Kreisch et al.* [2016]. Their single-scattering albedo spectrum was converted to  $R^*$  (radiance factor/ $\cos(i)$ ) using equation 10.5 of *Hapke* [2012] assuming isotropic scattering and using incidence and emission angles of the Hakos Mastcam observations (both  $38^\circ$ ). Although the CRISM spectrum is slightly redder in the visible wavelengths than the Hakos spectra, the overall  $R^*$  values and near-infrared spectral shape of the CRISM spectrum match well.

The four sieved samples generated at the Gobabeb site on Namib Dune included Dump samples A ( $<150 \mu\text{m}$ ), B ( $>150 \mu\text{m}$ ), C ( $150\text{--}1000 \mu\text{m}$ ), and D ( $>1000 \mu\text{m}$ ). Figure 16 is an enhanced M34 mosaic showing all four dumped samples, in which the finest fraction (Dump A) is substantially redder than the other samples and the background Gobabeb sands. Figure 17 shows the RMI images acquired of the four dump piles at various stages during the campaign (note that the APXS had touched the surface of Dump D prior to image acquisition). The corresponding ChemCam spectra from these locations are shown in Figure 18, along with a nearby undisturbed sand spectrum (Dwyka). Dump A exhibits the brightest near-infrared relative reflectance, with a peak near 750 nm followed a downturn. The Dump B spectrum is substantially different, with a flatter spectral slope between 600 nm and 700 nm followed by a more severe downturn longward of 700 nm. Although this downturn is similar to a weaker downturn present in Dwyka, the visible reflectance of Dump B is much higher and the peak reflectance position is shifted to shorter wavelengths than that for Dwyka. Dumps C and D are similar in spectral shape to Dump B but exhibit sequentially lower relative reflectance at wavelengths  $>550$  nm. These variations are likely not caused by photometric effects, as the phase angles of all Dump pile observations are between  $66^\circ$

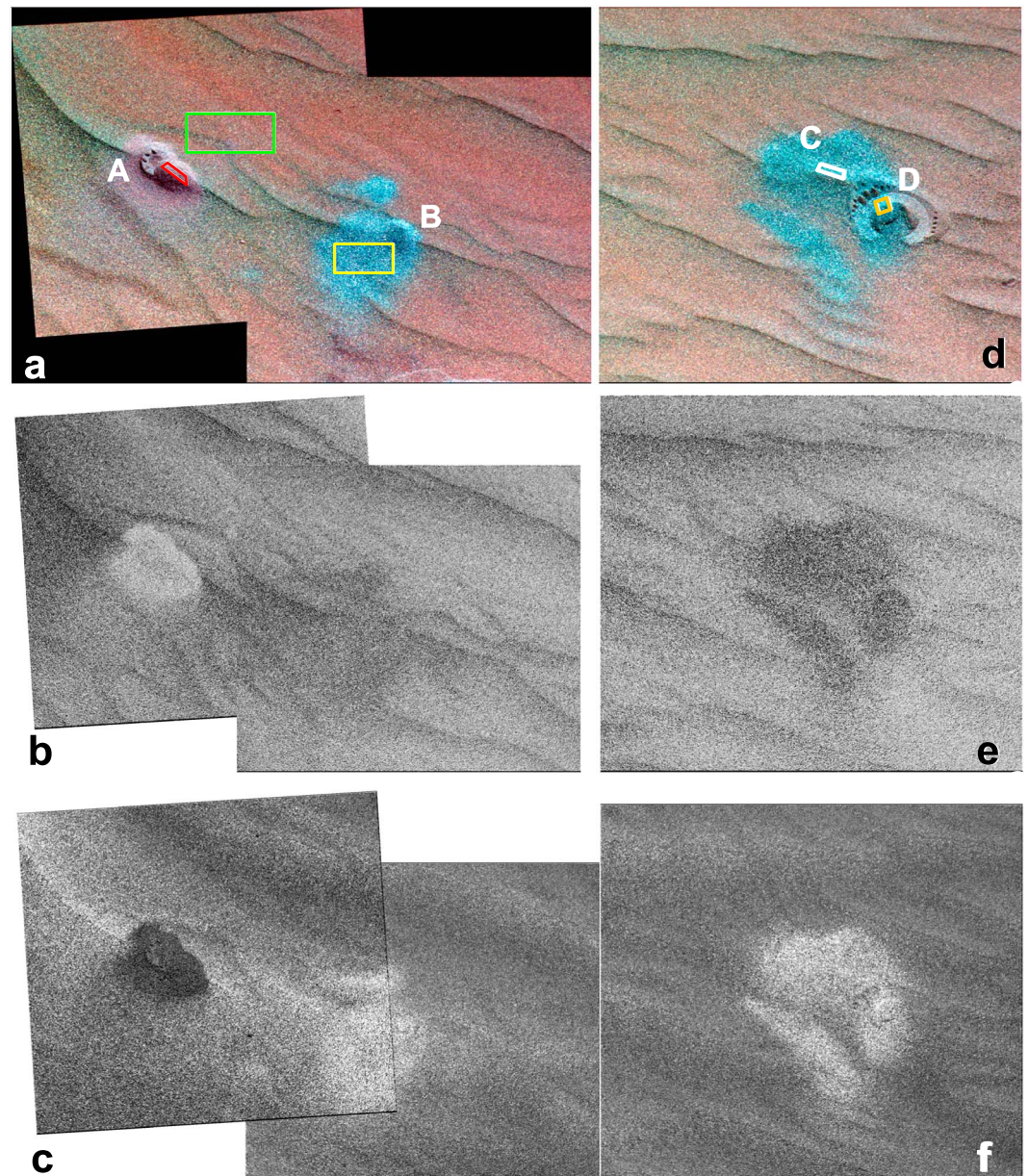


**Figure 19.** (a) False-color M100 mosaic (751, 527, and 445 nm) of Dump piles A and B from Sol 1229 (mcam05651 and mcam05652). Regions of interest from which Mastcam spectra were acquired (Figure 20) shown by boxes (green = undisturbed sand; red = Dump A; yellow = Dump B; white = Dump C; orange = Dump D). Dump A was imaged after the APXS touched the surface on Sol 1227. (b) 527 nm band depth mosaic. (c) 638/1013 nm ratio (using red Bayer filter and R6 filter). (d) False-color M100 (751, 527, and 445 nm) of Dump piles C and D from Sol 1234 (mcam05707). Regions of interest from which Mastcam spectra were acquired (Figure 20) shown by boxes. Dump area was imaged after the APXS touched the surface on Sol 1231. (e) 527 nm band depth mosaic. (f) 638/1013 nm ratio (using red Bayer filter and R6 filter). Dump A has a stronger 527 nm band depth and weaker 638/1013 nm ratio compared to Dumps B-D, consistent with its more ferric nature.

and 73°. Dwyka was acquired at a lower phase angle (30°), but this should only result in minor differences in overall reflectance values.

Mastcam multispectral observations of the Dump piles provide similar results. Figure 19a shows a false-color M100 mosaic of Dump A (imaged after an APXS touch) and Dump B, along with ROI locations (including an undisturbed area near Dump A). The 527 nm band depth image (Figure 19b) shows enhanced ferric absorptions in the finer-grained Dump A sample compared to Dump B and the surrounding Gobabeb sands. The 638/1013 nm ratio map in Figure 19c shows correspondingly low values for Dump A, consistent with a

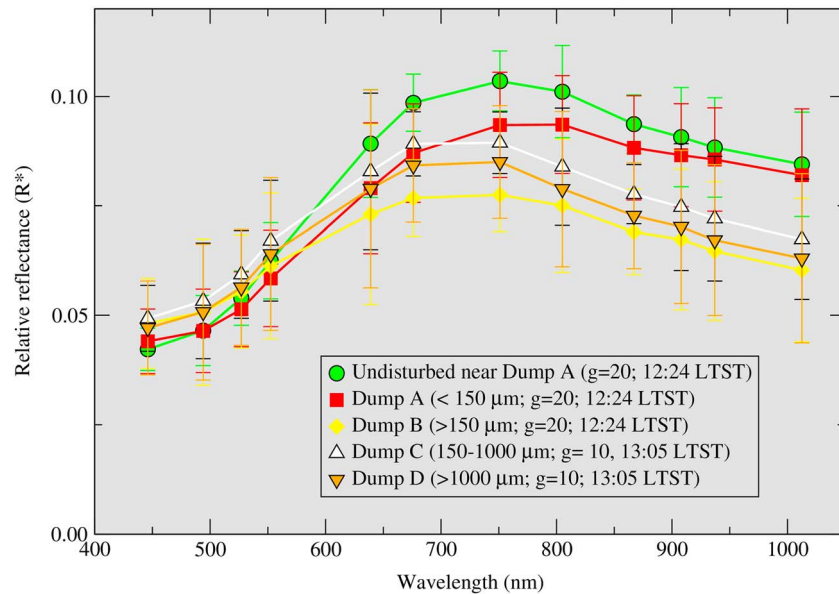


**Figure 20.** Mastcam spectra of Dump piles A–D, and from an undisturbed area near Dump A, color coded to ROI location shown in Figure 19. Error bars represent standard deviations within selected region of interest. Legend shows average phase angle ( $g$ ) and LTST time for each observation.

less steep near-infrared downturn compared to Dump B (as well as the background sands). Dumps C and D are shown as a false-color M100 image in Figure 19d (along with ROI locations). An APXS touch at the Dump D location occurred prior to this image acquisition. The 527 nm band depth and 638/1013 nm ratio maps (Figures 19e and 19f, respectively) show little variation between the two dumps but are distinctly less ferric than the background Gobabeb sands.

Figure 20 shows the Mastcam spectra of the four dump piles as well as the undisturbed background sand near Dump A. Similar to the ChemCam spectra, Dump A is distinct in its overall high near-infrared relative reflectance and shallower downturn. The spectral shapes of Dumps B, C, and D are similar, although Dump B exhibits the lowest near-infrared relative reflectance, which is inconsistent with the progressive darkening with increasing grain size observed in the ChemCam spectra. However, this may result from a photometric effect wherein the Dumps C and D spectra were acquired at phase angles  $\sim 10^\circ$  compared to  $\sim 20^\circ$  for Dumps A and B. Although the absolute difference is only  $\sim 10^\circ$ , the closer proximity of Dumps C and D to the opposition surge ( $0^\circ$ ) could result in higher relative reflectance.

After the rover departed the Gobabeb area, it deposited the Dumps E and F samples onto bedrock surfaces north of High Dune. Figure 21 shows the false-color M34 image of this area along with ROI mosaics of the dump piles. Dump F is darker in the 527 nm band depth image (Figure 21b) and brighter in the 640/1012 nm ratio map (Figure 21c), consistent with a less ferric nature compared to Dump E. The ChemCam and Mastcam spectra for these samples are shown in Figure 22, in which the larger grains in Dump F result in higher visible wavelength relative reflectances and lower near-infrared relative reflectances compared to the fine-grained Dump E sample. This is consistent with the results from the Gobabeb Dump samples shown in Figures 18 and 20. Although the comparison between the spectra acquired with the two instruments is excellent in the visible wavelengths ( $< 638$  nm), the Mastcam  $R^*$  values at longer wavelengths are higher. This is unlikely to be a photometric effect (phase angles are all  $\sim 6$ – $14^\circ$ ) but may result from different fields of view sampled between the measurements and/or differences between instrument calibration uncertainties.

## 6. Discussion

### 6.1. Overview of Results From Other MSL Instruments

The results of Bagnold Dune analyses from the other Curiosity payload instruments are presented in detail elsewhere in the Bagnold Dune Field Special Issue, but a brief summary of those results is useful for comparison to the

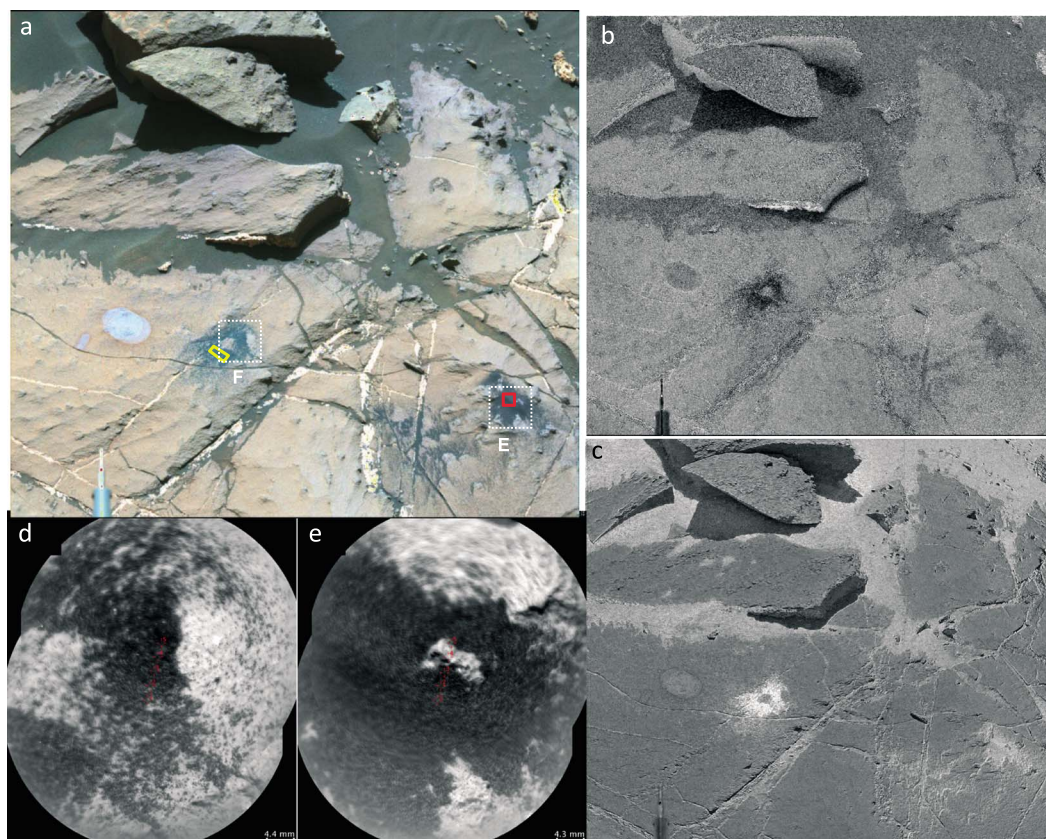


**Figure 21.** (a) False-color M34 image (751, 527, and 445 nm) of Dump piles E and F from Sol 1253 (mcam05852). Regions of interest from which Mastcam spectra were acquired (Figure 22) shown by boxes (red = Dump E; yellow = Dump F). Dotted white lines are approximate outlines of RMI mosaics. Bluish oval on bedrock to left of Dump F is brushed target “Kuisseb.” (b) 527 nm band depth mosaic. (c) 640/1012 nm ratio (using red Bayer filter and L6 filter). (d) RMI mosaic of Dump F. (e) RMI mosaic of Dump E. Dump F has a weak 527 nm band depth (dark tones) and strong 640/1012 nm ratio (light tone) compared to Dump E, consistent with its less ferric nature.

VNIR spectra shown here. The LIBS data from ChemCam showed that the sands associated with Bagnold Dunes exhibited similar major element abundances to typical soils. However, the sum of total oxides was higher than typical soils, while the hydrogen and other volatiles were lower, suggestive of less amorphous and/or less hydrated components. An apparent mixing relation was observed between the more felsic, finest grain size fractions and the more mafic, coarsest fractions, which exhibited higher Mg and increasing normative olivine content with grain size [Cousin *et al.*, 2017]. APXS measurements also suggested that the Namib/Gobabeb dune sands were enriched in Mg, particularly in the coarser fractions, whereas the High Dune sands were relatively more feldspathic [O’Connell-Cooper *et al.*, 2017]. All Bagnold Dune sands were similar to other Gale soils, in general, but with less dust (lower S and Cl). The coarsest Gobabeb samples were more mafic, consistent with the presence of more olivine (15 volume normative % within Dump D, according to APXS). The exception was the coarse crest sand Barby at High Dune, which was the most felsic sand.

ChemMin results of the Gobabeb <150  $\mu\text{m}$  size fraction revealed the crystalline portion to comprise the following minerals (and weight percents): andesine ( $36.5 \pm 8$ ), olivine ( $25.8 \pm 4$ ) of composition  $\text{Fo}_{55}$ , augite ( $22.0 \pm 4$ ), pigeonite ( $10.6 \pm 4$ ), magnetite ( $2.1 \pm 2$ ), anhydrite ( $1.3 \pm 1$ ), quartz ( $0.8 \pm 1$ ), and hematite ( $0.9 \pm 1$ ) as summarized by Achilles *et al.* [2017]. The amorphous component was substantial, however, at  $35 \pm 15\%$ , with a composition mainly of  $\text{SiO}_2$  (~50 wt %),  $\text{FeO}_7$  (~20 wt %),  $\text{Al}_2\text{O}_3$  (~8 wt %), and  $\text{SO}_3$  (~7 wt %). These results are somewhat similar to the Rocknest bed form results [Blake *et al.*, 2013], but Gobabeb contains ~5% more olivine, ~3% more augite, and 4% less plagioclase. However, the Rocknest sieved materials (<150  $\mu\text{m}$ ) were much finer grained than the corresponding sieved samples from Gobabeb [Ehlmann *et al.*, 2017; Minitti *et al.*, 2013].

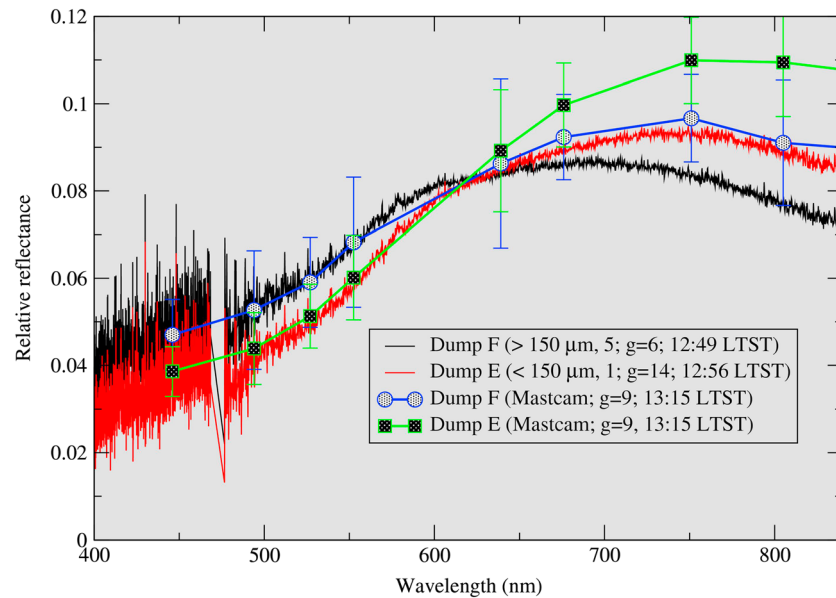


**Figure 22.** ChemCam spectra of presieve Dump F (>150  $\mu\text{m}$ ) and postsieve Dump E (<150  $\mu\text{m}$ ) Gobabeb Dune samples (raster location shown in parentheses) from Sol 1253 sequences ccam01253 and ccam02253, respectively (cf. Figure 21). Also shown are Mastcam  $R^*$  spectra from same Sol (mcam05852) acquired on Dumps E and F samples and at similar phase angles as ChemCam. Error bars represent standard deviations within selected region of interest. Legend shows average phase angle ( $g$ ) and LTST time for each observation.

SAM measurements were conducted on both the <150  $\mu\text{m}$  and 150–1000  $\mu\text{m}$  grain size fractions from Gobabeb. *Sutter et al.*, [2017] reported that SAM found a higher-temperature water release in the Namib sands related to a hydrated phase, although it was a smaller amount than observed in the Rocknest soil. They suggested that the greater surface area associated with finer-grained materials enabled greater retention of adsorbed water compared to coarser-grained materials. The <150  $\mu\text{m}$  sample saw  $\text{SO}_2$  release temperatures consistent with the presence of Mg sulfates, while the 150–1000  $\mu\text{m}$  sample saw  $\text{SO}_2$  release temperatures consistent with Fe sulfates. They noted that the nearby Murray mudstone outcrops contained intermittent Mg sulfate concretions [e.g., *Nachon et al.*, 2017] and jarosite [e.g., *Rampe et al.*, 2017] from which fragments could contribute to the Gobabeb sands.

Mars Hand Lens Imager (MAHLI) images of High Dune sands showed diverse relative colors, with darker sand grains dominant in the coarse fraction, sometimes mantled by finer dust. Opaque grains were relatively colorless (light toned to gray), while red and yellow hues were observed in more translucent grains. Darker grains were interpreted by *Ehlmann et al.* [2017] as basaltic, translucent yellow grains as feldspars and/or olivines, red grains as pieces of local Murray Formation mudstone or reddish soils (i.e., dust containing), and white grains as fragments of calcium sulfate veins. Images of the Barby crest showed medium to fine sands (mostly 100–300  $\mu\text{m}$  with some up to 900  $\mu\text{m}$ ), whereas the Kibnas trough particles were mainly <500  $\mu\text{m}$  and dominated by many smaller grains.

Finally, *Newman et al.* [2016] used observations from the Rover Environmental Monitoring Station to conclude that the overall wind pattern in the Bagnold Dunes showed daytime winds coming from between the northwest and northeast directions, consistent with previous results from orbital monitoring [*Ayoub et al.*, 2014; *Bridges et al.*, 2012a, 2012b; *Silvestro et al.*, 2013] They also found that winds transitioned at night to come from the southeast (dominated by the upslope-downslope flow from Mount Sharp).

## 6.2. Laboratory Sample Comparison

We combined the minerals and abundances reported by CheMin for the <150  $\mu\text{m}$  sample [*Achilles et al.*, 2017] via linear mixing (where spectra of representative minerals are weighted by their percent contribution) to allow a qualitative comparison to ChemCam spectra. Figure 23 shows laboratory spectra [*Clark et al.*, 2003] of representative minerals detected by CheMin, as well as a proxy for the amorphous component as

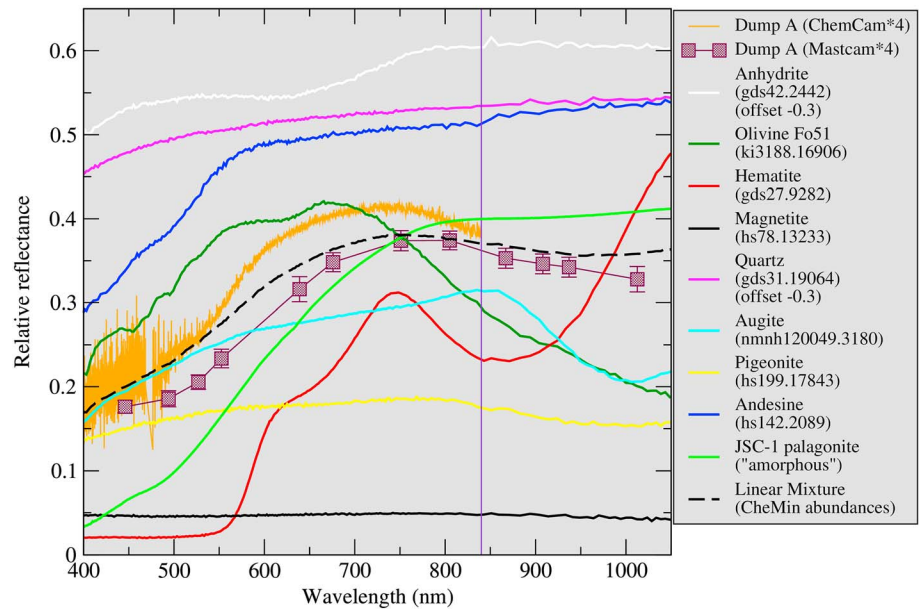


**Figure 23.** Laboratory spectra of minerals identified by CheMin in the Gobabeb  $<150\ \mu\text{m}$  sand fraction [cf. *Achilles et al.*, 2017; from *Clark et al.*, 2003], with sample identifiers and offsets noted in the legend. JSC-1 palagonite sample [Johnson and Grundy, 2001] is considered here as representative of the CheMin  $\sim 35\%$  amorphous component. ChemCam and Mastcam spectra of Dump A (Figures 18 and 20, respectively) have been multiplied by 4 for more direct comparison. Dashed line represents linear mixture of spectra weighted according to CheMin abundances. Vertical line at 840 nm represents ChemCam's wavelength extent.

represented by the JSC-1 Mars analog soil [cf. *Allen et al.*, 1998; *Johnson and Grundy*, 2001]. Also included in Figure 23 are the ChemCam and Mastcam Dump A spectra, multiplied by a factor of 4 to facilitate more direct comparison. Our computed linear mixture from these components is about a factor of 4 too high in reflectance compared to the ChemCam and Mastcam spectra of Bagnold Dunes, likely owing to the nonlinear mixing effects of opaque minerals. For example, the low reflectance, spectrally flat nature of magnetite provides a nonlinear, darkening contribution to spectra in the visible wavelength region without appreciably altering band widths or positions [e.g., *Singer*, 1981; *Cloutis et al.*, 2011]. In addition, the variable grain size distributions of the lab samples are likely somewhat different than the Martian samples. The overall spectral shape of the synthetic mixture spectrum is similar to the ChemCam and Mastcam spectra for Dump A, but spectrally flatter, without as deep a near-infrared downturn or ferric band near 535 nm. Only olivine and hematite exhibit near-infrared downturns beginning near 700–750 nm similar to those in ChemCam and Mastcam spectra of the dune sands, although the high-Ca pyroxene augite exhibits a downturn after  $\sim 850\ \text{nm}$  that contributes to the overall near-infrared dropoff.

Figure 24 presents laboratory spectra of the San Carlos forsterite ( $\text{Fo}_{90.4}$ ) that were sieved to the same grain sizes as the Gobabeb sieved samples. The decrease in reflectance with increasing grain size is apparent [cf. *King and Ridley*, 1987], although the 150–1000  $\mu\text{m}$  fraction is brighter than the  $>150\ \mu\text{m}$  fraction, likely owing to the presence of darker  $>1000\ \mu\text{m}$  grains in the  $>150\ \mu\text{m}$  fraction. Although this is opposite to the trend observed in the ChemCam spectra (Figure 18), it is consistent with the conclusions from MAHLI images that Gobabeb sands have few grains  $>1000\ \mu\text{m}$  [Ehlmann et al., 2017].

### 6.3. Spectral Parameters

Based on the spectra presented above, we computed several spectral parameters to distinguish trends among the Bagnold Dune samples. For ChemCam passive spectra, key among these are the slope and ratio between 600 nm and 440 nm, the 535 nm band depth, the 600/700 nm ratio, the 700/840 nm ratio, and the peak reflectance value. Figure 25a compares the 535 nm band depth to the 600/700 nm ratio for all ChemCam spectra, which shows a linear trend between coarse sieved, ferrous samples and fine-grained, ferric samples. Fine-grained materials have the highest 535 nm band depths and lower 600/700 nm ratios (higher relative reflectances at 700 nm than 600 nm), such as Arris\_Drift, Dwyka, portions of the Kibnas trough, and the disturbed

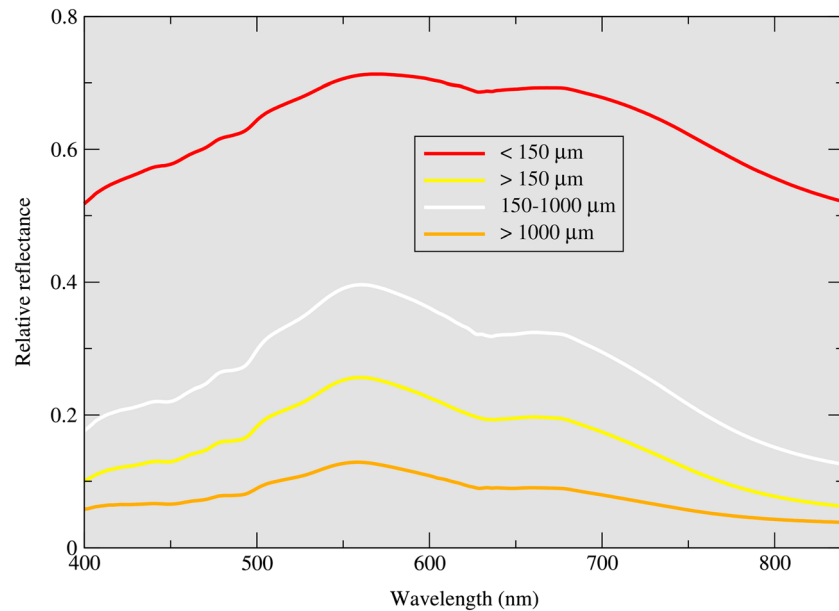


**Figure 24.** Laboratory spectra of San Carlos forsterite ( $\text{Fo}_{90.4}$ ) [see Cloutis *et al.*, 2006] sieved to same grain size fractions as Gobabeb samples, showing decreasing reflectance with increasing grain size.

soils at Awasib and Hoanib. The coarser sieved samples are less ferric and exhibit higher 600/700 nm ratios (flatter spectrum) and near-zero 535 nm band depths. The parameter values computed from the CRISM spectrum of Namib (Figure 15) are also included and fall midway between the end-member values. Figure 25b demonstrates another linear trend between the peak reflectance value and the 440 nm to 600 nm slope. In this case the brightest materials are also the reddest (Arris\_Drift, Karibib, Sinclair, and the CRISM spectrum), whereas the darkest and bluest materials correspond to the coarsest sieved samples. Figure 25c compares the 600/440 nm ratio to the 600/700 nm ratio, for which the reddest samples (Arris\_Drift, Sinclair, and Karibib) typically have lower 600/700 nm ratios. However, a second population of samples with similar 600/440 nm ratios but variable 600/700 nm ratios includes the  $<150 \mu\text{m}$  sieved sands and Awasib/Hoanib disturbed soils and also the Dwyka undisturbed sand and Kibnas trough. This may reveal a relatively constant abundance of ferric materials (similar 600/440 nm ratio) within these samples compared to more variable amounts of coarser, ferrous materials (as evidenced by the variable 600/700 nm ratios). A comparison of the 600/440 nm ratio to the 700/840 nm ratio in Figure 25d demonstrates that redder materials (high 600/400 nm ratios such as Arris\_Drift, Sinclair, and the CRISM spectrum) typically exhibit the lowest 700/840 nm ratios. This is consistent with their relative lack of stronger near-infrared downturns normally associated with ferrous materials in the coarsest sieved piles. However, the  $<150 \mu\text{m}$  sieved fractions and some disturbed sands again plot off this trend (toward less ferrous signatures for a given 600/440 nm ratio). It may be that at these finest grain size fractions, the spectra are dominated by the ferric components and mask the ferrous components that are documented in the CheMin results.

Mastcam spectral parameters shown in Figure 26a compare the band depth at 527 nm to the 676/751 nm ratio, for which the fine-grained samples again plot at higher band depths and lower ratio values compared to the coarser samples. The peak reflectance value versus the visible spectral slope (446 to 639 nm) shown in Figure 26b demonstrates, in general, that the darkest and bluest samples again correspond to the coarsest size fractions. The Hoanib samples appear to plot along a separate trend of higher peak reflectance than the other samples. This may result from the  $\sim 74^\circ$  phase angle at which these data were acquired, which was the highest of any Mastcam observation. The general forward scattering nature of dune and ripple sands will result in slightly elevated reflectances at these higher phase angles [cf. Johnson *et al.*, 2006]. The 639/446 nm ratio versus the 676/751 nm ratio (Figure 26c) and the 676/876 nm ratio (Figure 26d) exhibit similar trends in which the reddest materials with lower red/near-infrared ratios are typically the finer-grained samples or those disturbed samples dominated by such a component (e.g., Kubib soil, Hoanib disturbed soil, and Hakos disturbed and track sands).

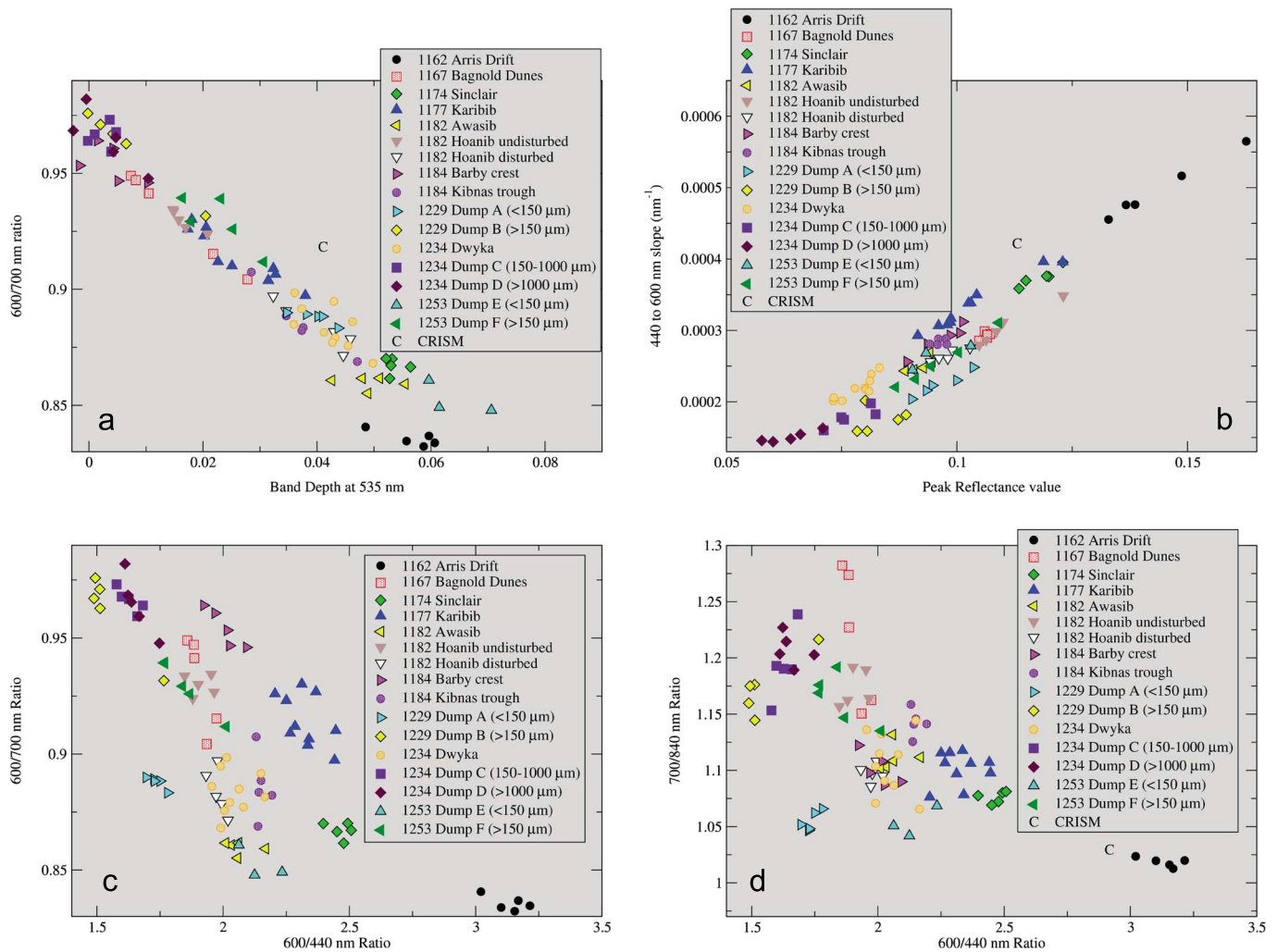


**Figure 25.** Spectral parameters computed from ChemCam passive spectra. (a) 535 nm band depth (computed between 500 and 600 nm) versus 600/700 nm ratio, (b) peak reflectance value versus 440 to 600 nm spectral slope, (c) 600/440 nm ratio versus 600/700 nm ratio, and (d) 600/440 nm ratio versus 700/840 nm ratio. Parameter values for CRISM spectrum of Namib area (Figure 15) are plotted except for Figure 25c where the value is (2.92, 0.92).

Dumps E and F exhibited more ferric spectral parameters (i.e., larger 535 nm (or 527 nm) band depths and 600/440 nm (or 639/446 nm) ratios) than their counterparts in Dumps A and B. This was unexpected, given that the grain size fractions were essentially identical between Dump A versus Dump E (<150 μm sieved fractions) and Dump B versus Dump F (>150 μm). Because the scoop locations were close to the rover and partially obscured by rover hardware, no Mastcam multispectral images were acquired. However, the MAHLI camera acquired a set of images of all three scoop locations on Sol 1241. Figure 27 shows a portion of a radiometrically calibrated, enhanced color MAHLI image in which the Scoop 3 interior (from which the Dumps E and F materials were obtained) appears redder than the other two scoops. A red/blue ratio constructed from the Bayer filters also demonstrates the less dark (less blue) nature of Scoop 3. This implies that the starting materials for Dumps E and F were slightly more ferric than the other dumped samples, which are borne out by their spectral parameters (Figures 25 and 26).

Because S content is known to correlate strongly with dust in soils [e.g., Yen et al., 2005; Berger et al., 2016], it is illustrative to examine how spectral parameters relate to S content measured by APXS [cf. Fraeman et al., 2015]. Visible region reflectance spectra are highly sensitive to the presence of oxide/hydroxide-bridged ferric iron atoms, including ferric iron-bearing sulfates [Sherman and Waite, 1985; Cloutis et al., 2006; Johnson et al., 2015a; Sklute et al., 2015]. Figure 28 shows the ChemCam 770/830 nm ratio compared to APXS S content for the Bagnold area samples [cf. O'Connell-Cooper et al., 2017]. The S content decreases

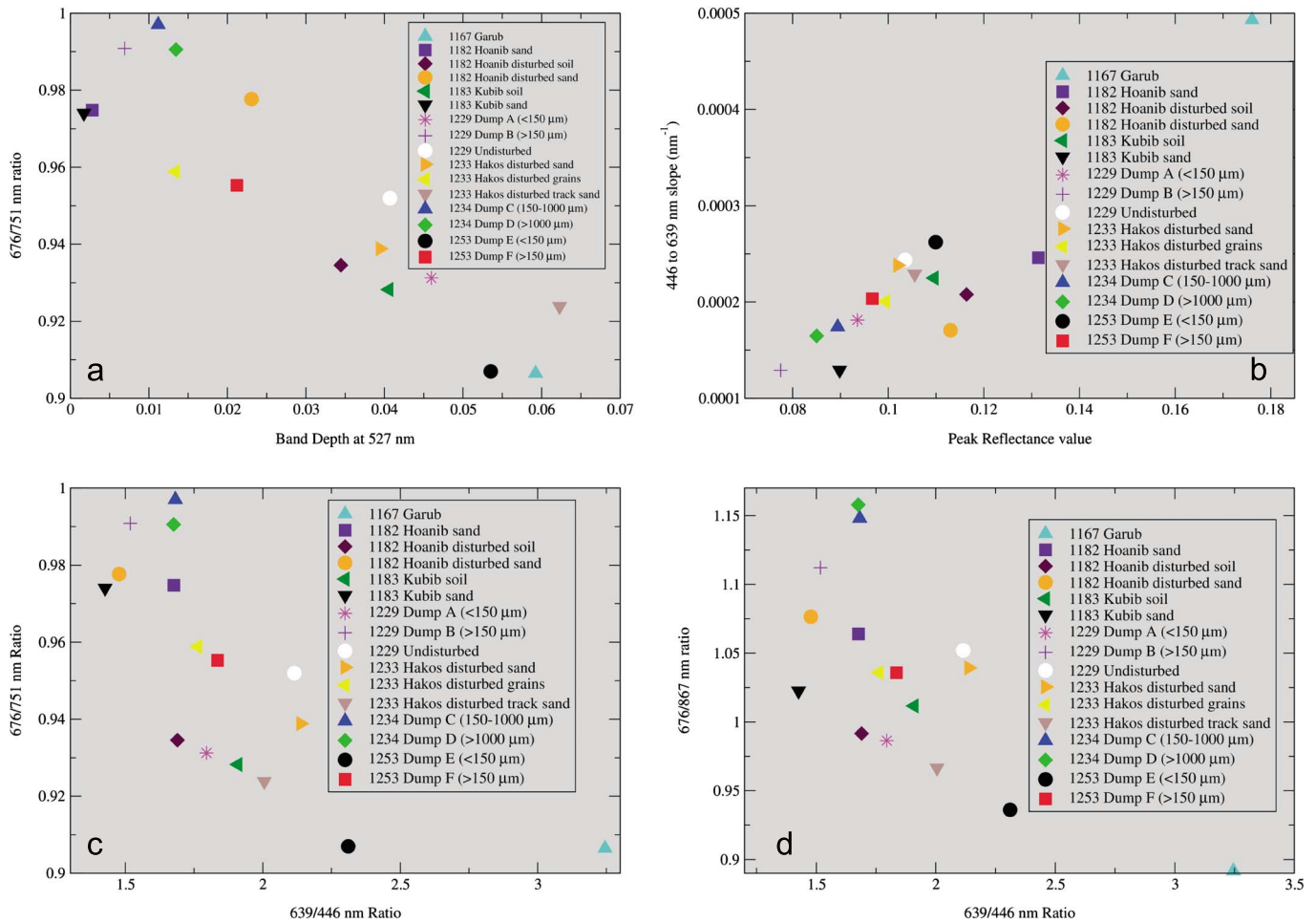


**Figure 26.** Spectral parameters computed from Mastcam spectra. (a) 527 nm band depth (computed between 494 and 639 nm bands) versus 676/751 nm ratio, (b) peak reflectance value versus 446 to 639 nm spectral slope, (c) 639/446 nm ratio versus 676/751 nm ratio, and (d) 639/446 nm ratio versus 676/867 nm ratio. See text for discussion.

with increasing grain size of the sieved samples, consistent with the loss of dust and/or finer-grained S-bearing sulfate minerals. The dustier undisturbed samples have systematically higher S, with the Barby crest sample exhibiting the highest S content overall and the Kibnas trough sample the lowest among the undisturbed samples.

**6.4. Mineral Segregation and Grain Sorting**

It is evident from Mastcam images acquired of the Bagnold Dune areas that brightness and color differences occur between the crests, troughs, and slopes of ripple forms at a variety of spatial scales (Figures 2, 4, 10, and 14). These result from differences in grain size and mineralogy, where the coarser, darker, and less red (bluer) grains are dominated by ferrous mafic minerals (principally olivine) and the finer, brighter, and redder grains contain sufficient ferric (and likely nanophase) materials to diminish the spectral features associated with the ferrous materials.

Variations in grain and mineral sorting have been studied extensively in terrestrial and planetary settings. Fedo et al. [2015] showed experimentally that the physical sorting of phenocrysts in basalt-derived sediments can result in olivine accumulation and associated increases in MgO, total Fe, with Al<sub>2</sub>O<sub>3</sub> depletion. Gao et al. [2016] used numerical studies to investigate dune growth and grain segregation mechanisms. They documented the formation of an armor of coarse grains on the top of bed forms and noted that when granular mixtures flow in small avalanches, systematic sorting occurs such that larger grains preferentially migrate to the top, whereas smaller grains tend to filter downward. This process, referred to as kinematic (or kinetic)

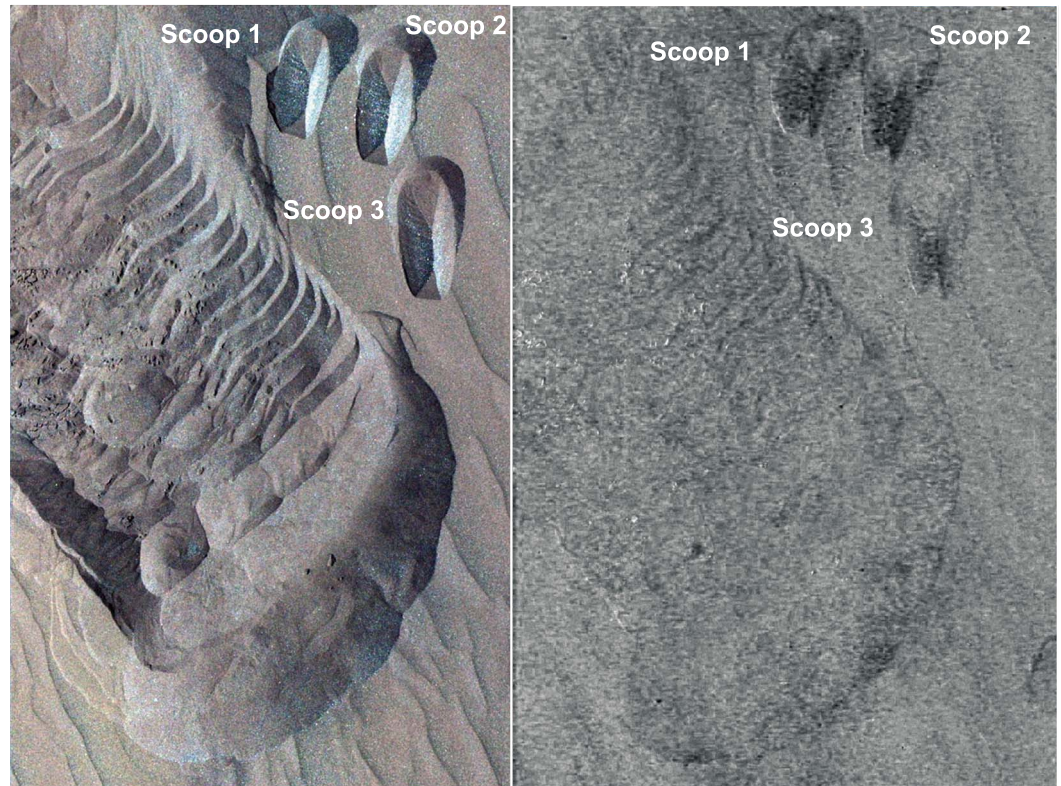


**Figure 27.** (left) Portion of Sol 1241 MAHLI image 1241MH0003900010403577E01\_DRXX showing location of scoops from which dump samples were acquired (Dumps A and B: Scoop 1; Dumps C and D: Scoop 2; Dumps E and F: Scoop 3). (right) Bayer filter red/blue ratio image for same region, demonstrating less dark (redder) materials in Scoop 3 compared to other scoops, consistent with spectral parameters in Figure 25.

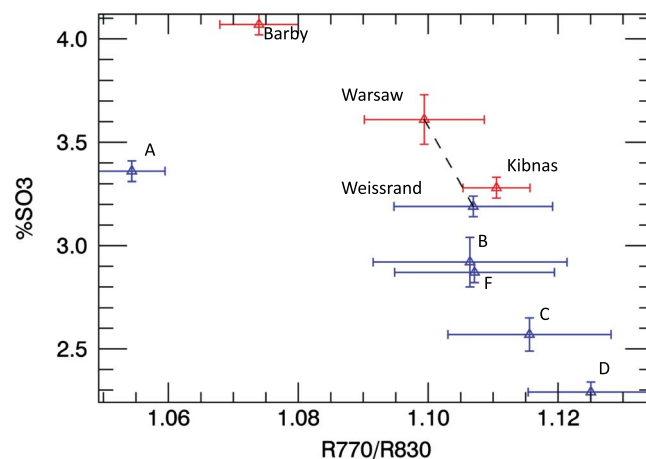


**Figure 28.** The average 770/830 nm ratios of ChemCam passive spectra versus APXS sulfur content. Blue symbols represent disturbed samples and red symbols undisturbed samples. Dump samples A–D and F labeled. The APXS target “Warsaw” was a nearby undisturbed target for comparison to Hoanib (1–5), whereas “Weissrand” represented the disturbed soil targets Hoanib (6–10) and Awasib. All spectral parameter values represent the median values  $\pm 5$  channels from the reported wavelength. Error bars represent standard deviations of 770/830 nm ratios and APXS precision.

sieving, is controlled by friction among grain surfaces and also results in collections of coarser grains at the base of sand piles [cf. *Kleinbans*, 2004]. *Jerolmack et al.* [2006] and *Sullivan et al.* [2008] noted that the ripples examined by the MER rovers exhibited such grain size sorting, with well-sorted coarse-grained crests and poorly sorted, generally finer-grained troughs. *Loope et al.* [2012] observed that grain flow strata in terrestrial Navajo Sandstone are typically coarsest at their base, consistent with grain sorting on the lee slopes of dunes. *Lapotre et al.* [2017] modeled grain size variations and showed coarser mafic minerals in the Bagnold dunes versus a nearby sand-filled hollow. *Pan and Rogers* [2017] used orbital data to note a positive correlation between olivine abundance and particle size within some spectrally heterogeneous sediment fields on Mars.

These characteristics are observed in many of the disturbed and undisturbed Bagnold Dune materials. Particularly noteworthy is the apparent armor of coarse grains observed in the Kubib area (Figure 8), below which occurred a redder, more ferric, fine-grained layer. Coarser, bluer grains were present intermittently at the base of the disturbed grain flows there as well. Color variations in the Barby/Kibnas area in Figure 10 also show redder, fine-grained materials in troughs between ripple forms and bluer, coarser materials along the crests. In the Hakos trench area (Figure 14) concentrations of coarse-grained, bluer materials occurred on the lee slopes of small ripples and in collections among the disturbed areas.

The visible/near-infrared spectra presented here support the concept of the Bagnold Dune sands comprising at least three components mixed to varying degrees: air fall dust, larger ferrous grains (dominantly olivine), and fine-grained, ferric material. Undisturbed sands can contain a mixture of dust and coarse- or fine-grained materials, depending on their position within a ripple form. For example, the Barby crest was a mixture of coarse ferrous and felsic grains, dust, and some S-bearing materials, whereas the redder Kibnas trough included more fine-grained, ferric materials. These ferric materials dominated the  $<150\ \mu\text{m}$  size fractions and likely included some minor S-bearing species (e.g., Ca/Mg/Fe sulfates), given the inverse correlation between S content and sieved sample grain sizes (Figure 28). The disturbed samples, in general, lack the dust component but are dominated either by the reddish materials (Hoanib and Awasib disturbed soils) or large grains (Hoanib undisturbed sand and Hakos disturbed sand grains). Conversely, the undisturbed samples are less influenced by the subsurface reddish soil but still are affected by air fall dust.

It is likely that dune migratory activity influences both surface and subsurface compositions. The magnitude of kinematic sieving may cause variations in proportions of coarse surficial grains relative to fine-grained, ferric materials that filter into the subsurface (e.g., compare Scoop 3 (Dumps E and F) to the others). Certainly, at the finest grain size fractions spectra are dominated by the ferric components, as characterized by their high 535 nm band depths and lower 600/700 nm ratios compared to the coarser samples (Figure 25). At High Dune, the Hoanib and Awasib disturbed sands and the Kubib subsurface layer exhibit spectral features indicative of more ferric components compared to the undisturbed surface sands and the larger-grained, bluer sands collected at the surface of grain flows.

## 7. Conclusions

Our combined use of ChemCam passive and Mastcam multispectral data offered a complementary perspective on the occurrence of iron-bearing minerals at Bagnold Dunes while supplementing and confirming data acquired by the other Curiosity payload instruments. As a reconnaissance tool, spectra acquired from a 140 m distance showed that the dunes exhibited features unlike previously observed targets. The combination of overall low relative reflectance, weak  $\sim 530\ \text{nm}$  absorption band, an absorption band near 620 nm, and a spectral downturn after  $\sim 685\ \text{nm}$  was consistent with olivine-bearing sands with likely contributions from high-calcium pyroxene (augite). Our detailed in situ investigations of the High Dune and Namib Dune areas demonstrated that a continuum of spectral features was present in the undisturbed and disturbed samples that occurred along the crest and within troughs of ripple forms. The finest grain size fractions typically exhibited the strongest  $\sim 530\ \text{nm}$  bands, highest relative reflectances, but lowest red/near-infrared ratios, consistent with a combination of ferric materials (hematite, magnetite, nanophase, and/or amorphous oxides). Conversely, the coarsest samples were the darkest and bluest, with strong downturns exhibited in the near-infrared, consistent with greater proportions of mafic minerals such as olivine and pyroxene. The collection of these sand grains along ridge crests, lee slopes, and among the upper surfaces of grain flows in disturbed materials is consistent with grain segregation via aeolian and/or kinematic sorting. Sorting also played a key role in populating the subsurface with fine-grained ferric components, as observed in disturbed sands and the  $<150\ \mu\text{m}$  sample population. These ferric materials may also serve to spectrally mask residual ferrous components. Indeed, we showed that while simple linear mixing of laboratory spectra using CheMin mineral abundances broadly replicated the overall shape of the ChemCam and Mastcam spectra, it could not replicate the low reflectance values or severity of the near-infrared downturns. This emphasizes the difficulties in using such methods to accurately model mineral abundances in visible/near-infrared wavelengths, particularly when comparing orbital data of natural surfaces to the  $<150\ \mu\text{m}$  grain size fraction ingested by CheMin.

Ongoing acquisition and analysis of visible/near-infrared point and imaging spectroscopy from ChemCam and Mastcam will be valuable as Curiosity continues its traverse through the southern extent of the Bagnold Dunes and toward the middle stratigraphic layers in Mount Sharp. Furthermore, in the likely event that landing sites for the upcoming Mars rovers encounter olivine-bearing sands, the in situ observations presented here and in the Bagnold Dune Field Special Issue will provide a critical baseline from which to compare hypotheses regarding sand provenance, segregation, and their impacts on sand mobilization on Mars.

#### Acknowledgments

This work was funded by the NASA Mars Science Laboratory Participating Scientist program through the Jet Propulsion Laboratory (contracts 1350588, 1449892, and 1546033). A portion of this research was carried out at the Jet Propulsion Laboratory, California Institute of Technology, under a contract with the National Aeronautics and Space Administration. The U.S. portion of ChemCam and MSL rover operations was funded by NASA's Mars Exploration Program. The French contribution to MSL is supported by the Centre National d'Etudes Spatiales (CNES). The authors thank Ray Arvidson (Washington University in St. Louis) for providing the CRISM spectrum of Namib Dune and Daniel Applin (University of Winnipeg) for spectra of sieved San Carlos samples. The authors thank the operations teams involved in acquiring these data sets, including the dedicated efforts of the payload uplink leads for the Mastcam and ChemCam teams. E.A.C. thanks NSERC, CSA, CFI, and MRIF for supporting the UW Planetary Spectrophotometer Facility at UW. Detailed reviews by D. Rogers and an anonymous reviewer helped clarify the presentation and analytical details of the manuscript. Original data that underlie the conclusions presented in this manuscript can be found on the NASA Planetary Data System and/or in the relevant references cited.

#### References

- Achilles, C. N., et al. (2017), Mineralogy of an active eolian sediment from the Namib Dune, Gale Crater, Mars *J. Geophys. Res. Planets*, *122*, doi:10.1002/2017JE005262.
- Allen, C. C., R. V. Morris, K. M. Jager, D. C. Golden, D. J. Lindstrom, M. M. Lindstrom, and J. P. Lockwood (1998), Martian regolith simulant JSC Mars-1, *Lunar Plan. Sci. Conf. XXIX*, #1690.
- Anderson, R., and J. Bell III (2010), Geologic mapping and characterization of Gale Crater and 601 implications for its potential as a Mars Science Laboratory site, *Mars*, *5*, 76–128, doi:10.1555/mars.2010.0004.
- Ayoub, F., J.-P. Avouac, C. E. Newman, M. I. Richardson, A. Lucas, S. Leprince, and N. T. Bridges (2014), Threshold for sand mobility on Mars calibrated from seasonal variations of sand flux, *Nat. Commun.*, *5*, doi:10.1038/ncomms6096.
- Banin, A., B. C. Clark, and H. Wanke (1992), Surface chemistry and mineralogy, in *Mars*, edited by H. H. Kieffer et al., pp. 594–625, Univ. of Ariz. Press, Tucson.
- Bell, J. F., et al. (2000), Mineralogic and compositional properties of Martian soil and dust: Results from Mars Pathfinder, *J. Geophys. Res.*, *105*(E1), 1721–1755, doi:10.1029/1999JE001060.
- Bell, J. F., III, et al. (2003), Mars exploration rover Athena Panoramic Camera (Pancam) investigation, *J. Geophys. Res.*, *108*(12), 8063, doi:10.1029/2003JE002070.
- Bell, J. F., III, et al. (2013), Initial multispectral imaging results from the Mars Science Laboratory Mastcam investigation at the Gale Crater field site. The 44th Lunar and Planet. Sci. Conf., LPI Contribution No. 1719, 1417.
- Berger, J. A., et al. (2016), A global Mars dust composition refined by the Alpha-Particle X-ray Spectrometer in Gale Crater, *Geophys. Res. Lett.*, *43*, 67–75, doi:10.1002/2015GL066675.
- Blake, D. F., et al. (2013), Curiosity at Gale crater, Mars: Characterization and analysis of the Rocknest sand shadow, *Science*, *341*(6153), 1239505.
- Bridges, N. T. and B. L. Ehlmann (2017), The Mars Science Laboratory (MSL) Bagnold Dunes campaign, Phase I: Overview and introduction to the special issue, *J. Geophys. Res. Planets*, *122*, doi:10.1002/2017JE005401.
- Bridges, N. T., F. Ayoub, J. P. Avouac, S. Leprince, A. Lucas, and S. Mattson (2012a), Earth-like sand fluxes on Mars, *Nature*, *485*(7398), 339–342.
- Bridges, N. T., et al. (2012b), Planet-wide sand motion on Mars, *Geology*, *40*(1), 31–34.
- Bristow, T. F., et al. (2015), The origin and implications of clay minerals from Yellowknife Bay, Gale crater, Mars, *Am. Mineral.*, *100*(4), 824–836.
- Clark, B. C., A. K. Baird, R. J. Weldon, D. M. Tsusaki, L. Schnabel, and M. P. Candelaria (1982), Chemical composition of Martian fines, *J. Geophys. Res.*, *87*, 10,059–10,067, doi:10.1029/JB087iB12p10059.
- Clark, R. N., et al. (2003), USGS Digital Spectral Library splib05a, *U.S. Geol. Surv. Open File Rep.*, 03–395.
- Cloutis, E. A., et al. (2006), Detection and discrimination of sulfate minerals using reflectance spectroscopy, *Icarus*, *184*, 121–157.
- Cloutis, E. A., P. Hudon, T. Hiroi, M. J. Gaffey, and P. Mann (2011), Spectral reflectance properties of carbonaceous chondrites: 2. CM chondrites, *Icarus*, *216*, 309–346.
- Cousin, A., et al. (2017), Geochemistry of the Bagnold dune field as observed by ChemCam and comparison with other aeolian deposits at Gale Crater, *J. Geophys. Res. Planets*, *122*, doi:10.1002/2017JE005261.
- Day, M., and G. Kocurek (2016), Observations of an aeolian landscape: From surface to orbit in Gale Crater, *Icarus*, *280*, 37–71, doi:10.1016/j.icarus.2015.09.042.
- Edgett, K. S., and P. R. Christensen (1994), Mars aeolian sand: Regional variations among dark-hued crater floor features, *J. Geophys. Res.*, *99*, 1997–2018, doi:10.1029/93JE03094.
- Ehlmann, B. L., and J. Buz (2015), Mineralogy and fluvial history of the watersheds of Gale, Knobel, and Sharp craters: A regional context for MSL Curiosity's exploration, *Geophys. Res. Lett.*, *42*, 264–273, doi:10.1002/2014GL062553.
- Ehlmann, B., et al. (2017), Chemistry, mineralogy, and grain properties at Namib and High dunes, Bagnold dune field, Gale crater, Mars: A synthesis of Curiosity rover observations, *J. Geophys. Res. Planets*, *122*, doi:10.1002/2017JE005267.
- Ewing, R. C., et al. (2017), Sedimentary processes of the Bagnold Dunes: Implications for the eolian rock record of Mars, *J. Geophys. Res. Planets*, *122*, doi:10.1002/2017JE005324.
- Fedo, C. M., I. O. McGlynn, and H. Y. McSween Jr. (2015), Grain size and hydrodynamic sorting controls on the composition of basaltic sediments: Implications for interpreting Martian soils, *Earth Planet. Sci. Lett.*, *423*, 67–77, doi:10.1016/j.epsl.2015.03.052.
- Fraeman, A. A., et al. (2015), Physical and material properties of Gale Crater sandy deposits: From Rocknest to Pahrump, In *Lunar Planet. Sci. Conf.*, vol. 46, abstract 1682.
- Gao, X., C. Narteau, and O. Rozier (2016), Controls on and effects of armoring and vertical sorting in aeolian dune fields: A numerical simulation study, *Geophys. Res. Lett.*, *43*, 2614–2622, doi:10.1002/2016GL068416.
- Geissler, P. E., and R. B. Singer (1992), Spectrophotometric mapping of Coprates Quadrangle, Mars. *Lunar Planet. Inst. Conf. Abstr.* 23, 403.
- Hanna, R. D., V. E. Hamilton, and N. E. Putzig (2016), The complex relationship between olivine abundance and thermal inertia on Mars, *J. Geophys. Res. Planets*, *121*, 1293–1320, doi:10.1002/2015JE004924.
- Hapke, B. (1993), *Theory of Reflectance and Emittance Spectroscopy*, pp. 455, Cambridge Univ. Press, Cambridge.
- Hapke, B. (2012), *Theory of Reflectance and Emittance Spectroscopy*, 2nd ed., pp. 520, Cambridge Univ. Press, Cambridge.
- He, X. D., K. E. Torrance, F. X. Sillion, and D. P. Greenberg (1991), A comprehensive physical model for light reflection Proceedings of the 18th Annual Conference on Computer Graphics and Interactive Techniques, 175–186.
- Hobbs, S. W., D. J. Paull, and M. C. Bourke (2010), Aeolian processes and dune morphology in Gale Crater, *Icarus*, *210*(1), 102–115, doi:10.1016/j.icarus.2010.06.006.

- Jerolmack, D. J., D. Mohrig, J. P. Grotzinger, D. A. Fike, and W. A. Watters (2006), Spatial grain size sorting in eolian ripples and estimation of wind conditions on planetary surfaces: Application to Meridiani Planum, Mars, *J. Geophys. Res.*, *111*, E12S02, doi:10.1029/2005JE002544.
- Johnson, J. R., and W. M. Grundy (2001), Visible/near-infrared spectra and two-layer modeling of palagonite-coated basalts, *Geophys. Res. Lett.*, *28*, 2101–2104, doi:10.1029/2000GL012669.
- Johnson, J. R., et al. (2006), Spectrophotometric properties of materials observed by Pancam on the Mars Exploration Rovers: 1. Spirit, *J. Geophys. Res.*, *111*, E02S14, doi:10.1029/2005JE002494.
- Johnson, J. R., et al. (2015a), ChemCam passive reflectance spectroscopy of surface materials at the Curiosity landing site, Mars, *Icarus*, *249*, 74–92, doi:10.1016/j.icarus.2014.02.028.
- Johnson, J. R., W. M. Grundy, M. T. Lemmon, J. F. Bell III, and R. G. Deen (2015b), Spectrophotometric properties of materials observed by Pancam on the Mars Exploration Rovers: 3. Sols 500–1525, *Icarus*, *248*, 25–71, doi:10.1016/j.icarus.2014.10.026.
- Johnson, J. R., et al. (2016), Constraints on iron sulfate and iron oxide mineralogy from ChemCam visible/near-infrared reflectance spectroscopy of Mt. Sharp basal units, Gale Crater, Mars, *Am. Mineral.*, *101*, 1501–1514.
- Kinch, K. M., J. F. Bell III, W. Goetz, J. R. Johnson, J. Joseph, M. B. Madsen, and J. Sohl-Dickstein (2015), Dust deposition on the decks of the Mars Exploration Rovers: 10 years of dust dynamics on the Panoramic Camera calibration targets, *Earth Space Sci.*, *2*, 144–172, doi:10.1002/2014EA000073.
- King, T. V. V., and W. I. Ridley (1987), Relation of the spectroscopic reflectance of olivine to mineral chemistry and some remote sensing implications, *J. Geophys. Res.*, *92*, 11,457–11,469, doi:10.1029/JB092iB11p11457.
- Kleinhans, M. G. (2004), Sorting in grain flows at the lee side of dunes, *Earth Sci. Rev.*, *65*, 75–102.
- Koeppen, W. C., and V. E. Hamilton (2008), Global distribution, composition, and abundance of olivine on the surface of Mars from thermal infrared data, *J. Geophys. Res.*, *113*, E05001, doi:10.1029/2007JE002984.
- Kreisch, C. D., J. A. O'Sullivan, R. E. Arvidson, D. V. Polite, L. He, N. T. Stein, J. Finkel, E. A. Guinness, M. J. Wolff, and M. G. A. Lapotre (2016), Regularization of Mars Reconnaissance Orbiter CRISM along-track oversampled hyperspectral imaging observations of Mars, *Icarus*, *282*, 136–151.
- Lane, M. D., and P. R. Christensen (2013), Determining olivine composition of basaltic dunes in Gale Crater, Mars, from orbit: Awaiting ground truth from Curiosity, *Geophys. Res. Lett.*, *40*, 3517–3521, doi:10.1002/grl.50621.
- Lapotre, M. G. A., et al. (2016), Large wind ripples on Mars: A record of atmospheric evolution, *Science*, *353*(6294), 55–58, doi:10.1126/science.aaf3206.
- Lapotre, M. G. A., B. L. Ehlmann, S. E. Minson, R. E. Arvidson, F. Ayoub, A. A. Fraeman, R. C. Ewing, and N. T. Bridges (2017), Compositional variations in sands of the Bagnold Dunes, Gale crater, Mars, from visible-shortwave infrared spectroscopy and comparison with ground truth from the Curiosity rover, *J. Geophys. Res. Planets*, *122*, doi:10.1002/2016JE005133.
- Le Mouélic, S., et al. (2015), The ChemCam Remote Micro-Imager at Gale crater: Review of the first year of operations on Mars, *Icarus*, *249*, 93–107.
- Loepe, D. B., J. F. Elder, and M. R. Sweeney (2012), Downslope coarsening in aeolian grain flows of the Navajo Sandstone, *Sediment. Geol.*, *265*, 156–162.
- Maurice, S., et al. (2012), The ChemCam instrument suite on the Mars Science Laboratory (MSL) rover: Science objectives and mast unit description, *Space Sci. Rev.*, *170*, 95–166, doi:10.1007/s11214-012-9912-2.
- Maurice, S., et al. (2016), ChemCam activities and discoveries during the nominal mission of Mars Science Laboratory in Gale crater, Mars, *J. Anal. At. Spectrom.*, doi:10.1039/c5ja00417a.
- McSween, H. Y., I. O. McGlynn, and A. D. Rogers (2010), Determining the modal mineralogy of Martian soils, *J. Geophys. Res.*, *115*, E00F12, doi:10.1029/2010JE003582.
- Milliken, R. E., J. P. Grotzinger, and B. J. Thomson (2010), Paleoclimate of Mars as captured by the stratigraphic record in Gale Crater, *Geophys. Res. Lett.*, *37*, L04201, doi:10.1029/2009GL041870.
- Minitti, M. E., et al. (2013), MAHLI at the Rocknest sand shadow: Science and science-enabling activities, *J. Geophys. Res. Planets*, *118*, 2338–2360, doi:10.1002/2013JE004426.
- Morris, R. V., D. C. Golden, and J. F. Bell III (1997), Low-temperature reflectivity spectra of red hematite and the color of Mars, *J. Geophys. Res.*, *102*, 912–9133, doi:10.1029/96JE03993.
- Morris, R. V., et al. (2000), Mineralogy, composition, and alteration of Mars Pathfinder rocks and soils: Evidence from multispectral, elemental, and magnetic data on terrestrial analogue, SNC meteorite, and Pathfinder samples, *J. Geophys. Res.*, *105*, 1757–1817, doi:10.1029/1999JE001059.
- Morris, R. V., et al. (2006), Mössbauer mineralogy of rock, soil, and dust at Meridiani Planum, Mars: Opportunity's journey across sulfate-rich outcrop, basaltic sand and dust, and hematite lag deposits, *J. Geophys. Res.*, *111*, E12S15, doi:10.1029/2006JE002791.
- Morris, R. V., et al. (2008), Iron mineralogy and aqueous alteration from Husband Hill through Home Plate at Gusev Crater, Mars: Results from the Mossbauer instrument on the Spirit Mars Exploration Rover, *J. Geophys. Res.*, *113*, E12S42, doi:10.1029/2008JE003201.
- Murchie, S., et al. (2007), Compact Reconnaissance Imaging Spectrometer for Mars (CRISM) on Mars Reconnaissance Orbiter (MRO), *J. Geophys. Res.*, *112*, E05S03, doi:10.1029/2006JE002682.
- Nachon, M., et al. (2017), Chemistry of diagenetic features analyzed by ChemCam at Pahrump Hills, Gale crater, Mars, *Icarus*, *281*, 121–136.
- Newman, C. E., et al. (2016), Winds measured by the Rover Environmental Monitoring Station (REMS) during the Mars Science Laboratory (MSL) rover's Bagnold Dunes Campaign and comparison with numerical modeling using MarsWRF, *Icarus*, doi:10.1016/j.icarus.2016.12.016.
- O'Connell-Cooper, C. D., J. G. Spray, L. M. Thompson, R. Gellert, J. A. Berger, N. I. Boyd, E. D. Desouza, G. M. Perrett, M. Schmidt, and S. J. VanBommel (2017), APXS-derived chemistry of the Bagnold dune sands: Comparisons with Gale Crater soils and the global Martian average, *J. Geophys. Res. Planets*, *122*, doi:10.1002/2017JE005268.
- Pan, C., and A. D. Rogers (2017), Occurrence and scale of compositional heterogeneity in Martian dune fields: Toward understanding the effects of aeolian sorting on Martian sediment compositions, *Icarus*, *282*, 56–69, doi:10.1016/j.icarus.2016.09.021.
- Pommerol, A., N. Thomas, B. Jost, P. Beck, C. Okubo, and A. S. McEwen (2013), Photometric properties of Mars soils analogs, *J. Geophys. Res. Planets*, *118*, 2045–2072, doi:10.1002/jgre.20158.
- Rampe, E. B., et al. (2017), Mineralogy of an ancient lacustrine mudstone succession from the Murray formation, Gale crater, Mars, *Earth Planet. Sci. Lett.*, doi:10.1016/j.epsl.2017.04.021.
- Rogers, A. D., and J. L. Bandfield (2009), Mineralogical characterization of Mars Science Laboratory candidate landing sites from THEMIS and TES data, *Icarus*, *203*(2), 437–453, doi:10.1016/j.icarus.2009.04.020.
- Rogers, A. D., and O. Aharonson (2008), Mineralogical composition of sands in Meridiani Planum determined from Mars Exploration Rover data and comparison to orbital measurements, *J. Geophys. Res.*, *113*, E06S14, doi:10.1029/2007JE002995.

- Rogers, A. D., and V. E. Hamilton (2015), Compositional provinces of Mars from statistical analyses of TES, GRS, OMEGA, and CRISM data, *J. Geophys. Res. Planets*, *120*, 62–91, doi:10.1002/2014JE004690.
- Sautter, V., et al. (2016), Magmatic complexity on early Mars as seen through a combination of orbital, in-situ and meteorite data, *Lithos*, *254*, 36–52.
- Schröder, S. E., Y. Grynko, A. Pommerol, H. U. Keller, N. Thomas, and T. L. Roush (2014), Laboratory observations and simulations of phase reddening, *Icarus*, *239*, 201–216.
- Seelos, K. D., F. P. Seelos, C. E. Viviano-Beck, S. L. Murchie, R. E. Arvidson, B. L. Ehlmann, and A. A. Fraeman (2014), Mineralogy of the MSL Curiosity landing site in Gale crater as observed by MRO/CRISM, *Geophys. Res. Lett.*, *41*, 4880–4887, doi:10.1002/2014GL060310.
- Sherman, D. M., and T. D. Waite (1985), Electronic spectra of Fe<sup>3+</sup> oxides and oxide hydroxides in the near IR to near UV, *Am. Mineral.*, *70*, 1262–1269.
- Silvestro, S., D. A. Vaz, R. C. Ewing, A. P. Rossi, L. K. Fenton, T. I. Michaels, J. Flahaut, and P. E. Geissler (2013), Pervasive aeolian activity along rover Curiosity's traverse in Gale Crater Mars, *Geology*, *41*(4), 483–486.
- Silvestro, S., D. A. Vaz, H. Yizhaq, and F. Esposito (2016), Dune-like dynamic of Martian Aeolian large ripples, *Geophys. Res. Lett.*, *43*, 8384–8389, doi:10.1002/2016GL070014.
- Singer, R. B. (1981), Near-infrared spectral reflectance of mineral mixtures: Systematic combinations of pyroxenes, olivine, and iron oxides, *J. Geophys. Res.*, *86*(B9), 7967–7982, doi:10.1029/JB086iB09p07967.
- Sklute, E. C., H. B. Jensen, A. D. Rogers, and R. J. Reeder (2015), Morphological, structural, and spectral characteristics of amorphous iron sulfates, *J. Geophys. Res. Planets*, *120*, 809–830, doi:10.1002/2014JE004784.
- Sullivan, R., et al. (2008), Wind-driven particle mobility on Mars: Insights from Mars Exploration Rover observations at “El Dorado” and surroundings at Gusev Crater, *J. Geophys. Res.*, *113*, E06507, doi:10.1029/2008JE003101.
- Sutter, B. et al (2017), Evolved gas analyses of sedimentary rocks and eolian sediment in Gale Crater, Mars: Results of the Curiosity rover's sample analysis at Mars instrument from Yellowknife Bay to the Namib Dune, *J. Geophys. Res. Planets*, *122*, doi:10.1002/2016JE005225.
- Toulmin, P., III, A. K. Baird, B. C. Clark, K. Keil, H. J. Rose Jr., R. P. Christian, P. H. Evans, and W. C. Kelliher (1977), Geochemical and mineralogical interpretation of the Viking inorganic chemical results, *J. Geophys. Res.*, *82*, 4625–4634, doi:10.1029/JS082i028p04625.
- Treiman, A. H., et al. (2016), Mineralogy, provenance, and diagenesis of a potassic basaltic sandstone on Mars: CheMin X-ray diffraction of the Windjana sample (Kimberley area, Gale Crater), *J. Geophys. Res. Planets*, *121*, 75–106, doi:10.1002/2015JE004932.
- Vaniman, D. T., et al. (2014), Mineralogy of a mudstone at Yellowknife Bay, Gale Crater, Mars, *Science*, *343*(6169), doi:10.1126/science.1243480.
- Wellington, D., J. Bell, J. Johnson, K. Kinch, M. Rice, A. Fraeman (2016), Visible and near-infrared spectra of select high-interest science targets within Gale Crater observed by MSL Mastcam, *Am. Mineral.*, doi:10.2138/am-2017-5760CCBY.
- Wiens, R. C., et al. (2013), Pre-flight calibration and initial data processing for the ChemCam laser-induced breakdown spectroscopy instrument on the Mars Science Laboratory rover, *Spectrochim. Acta, Part B*, *82*, 1–27.
- Wiens, R. C., S. Maurice, and the MSL Science Team ChemCam (2015), Chemostratigraphy by the first Mars microprobe, *Elements*, *11*(1), 33–38, doi:10.2113/gselements.11.1.33.
- Wiens, R., et al. (2012), The ChemCam instrument suite on the Mars Science Laboratory (MSL) rover: Body unit and combined system performance, *Space Sci. Rev.*, *170*, 167–227.
- Yen, A. S., et al. (2005), An integrated view of the chemistry and mineralogy of Martian soils, *Nature*, *436*(7047), 49–54.